J. Fluid Mech. (2012), *vol.* 712, *pp.* 169–202.
doi:10.1017/jfm.2012.408

Parametric forcing approach to rough-wall turbulent channel flow

A. Busse† and N. D. Sandham

Aerodynamics and Flight Mechanics Research Group, Faculty of Engineering and the Environment, University of Southampton, Southampton SO17 1BJ, UK

(Received 8 March 2012; revised 7 June 2012; accepted 8 August 2012; first published online 27 September 2012)

The effects of rough surfaces on turbulent channel flow are modelled by an extra force term in the Navier–Stokes equations. This force term contains two parameters, related to the density and the height of the roughness elements, and a shape function, which regulates the influence of the force term with respect to the distance from the channel wall. This permits a more flexible specification of a rough surface than a single parameter such as the equivalent sand grain roughness. The effects of the roughness force term on turbulent channel flow have been investigated for a large number of parameter combinations and several shape functions by direct numerical simulations. It is possible to cover the full spectrum of rough flows ranging from hydraulically smooth through transitionally rough to fully rough cases. By using different parameter combinations and shape functions, it is possible to match the effects of different types of rough surfaces. Mean flow and standard turbulence statistics have been used to compare the results to recent experimental and numerical studies and a good qualitative agreement has been found. Outer scaling is preserved for the streamwise velocity for both the mean profile as well as its mean square fluctuations in all but extremely rough cases. The structure of the turbulent flow shows a trend towards more isotropic turbulent states within the roughness layer. In extremely rough cases, spanwise structures emerge near the wall and the turbulent state resembles a mixing layer. A direct comparison with the study of Ashrafian, Andersson & Manhart (*Intl J. Heat Fluid Flow*, vol. 25, 2004, pp. 373–383) shows a good quantitative agreement of the mean flow and Reynolds stresses everywhere except in the immediate vicinity of the rough wall. The proposed roughness force term may be of benefit as a wall model for direct and large-eddy numerical simulations in cases where the exact details of the flow over a rough wall can be neglected.

Key words: topographic effects, turbulent boundary layers, turbulence simulations

1. Introduction

Rough surfaces influence the behaviour of turbulent fluid flow in many technical applications and geophysical situations. Roughness may occur due to imperfections in the production process, such as in industrial steel pipes (see Langelandsvik, Kunkel & Smits (2008) and references therein), because the costs of obtaining a perfectly smooth surface would be uneconomic. In other cases a surface is made deliberately rough in

† Email address for correspondence: a.busse@soton.ac.uk

order to improve the flow properties over it, as in the case of riblets (see Karniadakis & Choi (2003) and references therein) or superhydrophobic surfaces (Rothstein 2010). In the geophysical context, a rich variety of rough surfaces is encountered, ranging from plant canopies (Finnigan 2000) to urban roughnesses (Cheng & Castro 2002; Coceal & Belcher 2005), which can influence regional climate (Arnfield 2003).

The most important effect of roughnesses on a turbulent boundary layer is a change in the mean velocity profile near the wall, which is expressed in the classical framework (Nikuradse 1950; Hama 1954; Schlichting 1968) using the (Hama) roughness function ΔU^+,

$$\langle u^+(z)\rangle = \kappa^{-1}\ln(z^+) + A - \Delta U^+(k^+), \tag{1.1}$$

where $\kappa \approx 0.4$ is the Kármán constant and $A \approx 5.5$ is the additive constant for a smooth-wall turbulent pipe flow (Schlichting 1968). The roughness function $\Delta U^+(k^+)$ is a function of the height of the roughness elements k^+. Flows over rough walls are usually classified as 'hydraulically smooth' when the height of the roughness elements is so small that they do not influence the viscous sublayer significantly, as 'transitionally rough' when the roughness elements begin to affect the buffer-layer viscous cycle, and the friction factor depends on both roughness height and viscosity, and as 'fully rough' when the roughness elements are so high as to completely destroy the buffer layer, and the friction factor becomes independent of viscosity (Schlichting 1968; Jiménez 2004).

For comparison of the aerodynamical properties of rough surfaces, it is common to use an equivalent sand grain roughness (Schlichting 1968), which is obtained in practice by fitting the asymptotic behaviour in the fully rough regime. Although this ensures a collapse of all roughness functions in the fully rough regime, the equivalent sand grain roughness is not sufficient to characterize the roughness function in the transitionally rough region (Jiménez 2004; Marusic *et al.* 2010). As the equivalent sand grain roughness is interchangeable with the roughness function (Jiménez 2004), it contains no information on the mean flow statistics beyond the shift in the velocity profile and no information at all about the fluctuation statistics of a rough-wall flow. For a more concise classification of rough surfaces, a parametrization that goes beyond the equivalent sand grain roughness is needed (Marusic *et al.* 2010).

Flow over rough surfaces has been investigated in the past predominantly by experiments. In recent years an increasing number of direct numerical simulations of turbulent flow over rough surfaces have been conducted in which the rough surface has been fully resolved either by a body-fitted grid (see e.g. Choi, Moin & Kim 1993; DeAngelis, Lombardi & Banerjee 1997; Coceal & Belcher 2005) or by immersed boundary methods (see e.g. Bhaganagar, Kim & Coleman 2004; Breugem & Boersma 2005; Leonardi & Castro 2010; Lee, Sung & Krogstad 2011). A full resolution of the rough surface considerably increases the computational costs compared to the smooth-wall case. Therefore the investigation of roughness effects has concentrated on simple geometries such as channel flow and flat-plate boundary layers. The numerical methods for resolving the rough surface are not free of difficulties. Body-fitted grids are limited to fairly regular geometries, while immersed boundary methods typically require a considerably higher number of grid points to resolve the near-wall turbulent flow (Iccarino & Verzicco 2003; Mittal & Iccarino 2005). No matter what method is employed, the simulation of a flow over a rough surface will always necessitate a much higher computational effort than the simulation of a comparable flow over a smooth surface. Direct numerical simulations of turbulent flows over more complex

rough surfaces such as plant canopies, where the plant canopies are fully resolved and their flexibility is taken into account, are probably still beyond the power of modern supercomputers.

Therefore, for numerical simulations of flows both in more complex geometries and over more complex roughness types, a simple way of modelling the effects of a rough surface would be desirable. Different approaches to the modelling of rough surfaces have been made where either the boundary conditions on the wall (Tuck & Kouzoubov 1995; Orlandi *et al.* 2003; Flores & Jiménez 2006) or the Navier–Stokes equations in the near-wall region are modified (Cui, Patel & Lin 2003; Breugem & Boersma 2005; Scotti 2006; Anderson & Meneveau 2010). In the context of the Reynolds-averaged Navier–Stokes equations, models based on a discrete element approach have been employed to capture roughness effects (Taylor, Coleman & Hodge 1985).

Here, the second approach is used by introducing an extra force term in the Navier–Stokes equations to model the effects of rough surfaces on the flow. The effects of the proposed roughness force term are explored by an extensive parameter study using direct numerical simulations. The results are compared to experimental and numerical studies of flow over rough surfaces.

The aim of this study is two-fold in advancing both the development of a numerical model of rough surfaces in the context of large-eddy simulations (LES) as well as the classification of rough surfaces by quantifying the effects of different parameters in the model. By looking at the mean flow as well as the turbulence statistics, we show to what extent a rough-wall turbulent flow can be represented by such a simple model and where this model falls short of the experimental reality.

This article is organized as follows. In § 2 the proposed roughness force term is discussed. A short description of the numerical methods employed is given in § 3. In § 4 standard mean flow and turbulence statistics are used to compare the direct numerical simulations containing the roughness force terms to results of experimental and numerical studies. In § 5 an example of a direct quantitative comparison is shown. The last section contains a final discussion of the results and concludes this article.

2. The roughness force term

When a fluid flows over a rough surface, in addition to the skin-friction drag at the wall, it experiences a pressure drag due to the extension of the roughness elements into the flow. Instead of fully resolving the rough surface, an extra force term is added to the Navier–Stokes equations to account for the additional pressure drag induced by the roughness elements. The forcing term is defined using a Cartesian coordinate system $(\boldsymbol{x}_1, \boldsymbol{x}_2, \boldsymbol{x}_3)$ whose coordinate axes are determined by the local mean flow and the wall geometry. Axis $\boldsymbol{x}_1$ points in the local mean flow direction parallel to the wall. In the following it is assumed that the wall is at rest; if this is not the case, the relative velocity to the wall should be used. Axis $\boldsymbol{x}_3$ indicates the wall-normal direction. The remaining axis $\boldsymbol{x}_2$ points in the spanwise direction in the plane of the wall.

In the case of a plane channel flow with a constant mean pressure gradient – the flow configuration studied in this paper – these are simply the streamwise, wall-normal and spanwise directions. The Navier–Stokes equations, non-dimensionalized by the channel half-width δ and the friction velocity u_τ and extended by the roughness force

term, then take the form

$$\frac{\partial u_i}{\partial t} + \frac{\partial u_i u_\beta}{\partial x_\beta} = \delta_{1i} - \frac{\partial p}{\partial x_i} + \frac{1}{Re_\tau}\frac{\partial^2 u_i}{\partial x_\beta \partial x_\beta} - \alpha_i F_i(z, h_i) u_i |u_i|, \tag{2.1}$$

$$\frac{\partial u_\beta}{\partial x_\beta} = 0. \tag{2.2}$$

Note that the summation convention is applied in this paper to Greek subscripts only; u_i $(i = 1, 2, 3)$ is used interchangeably with u, v, w to denote the streamwise, spanwise and wall-normal velocity components; and x_i $(i = 1, 2, 3)$ with x, y, z to denote the streamwise, spanwise and wall-normal coordinates.

The pressure gradient is split into the constant mean streamwise pressure gradient, $-\delta_{1i}$, and its fluctuating part $\partial p/\partial x_i$. The Reynolds number based on the friction velocity is defined by $Re_\tau = u_\tau \delta/\nu$. Note that the friction velocity and length scales used in the following are based on the mean streamwise pressure gradient,

$$u_\tau^2 = -\frac{\delta}{\rho}\frac{\mathrm{d}P}{\mathrm{d}x} = 1, \tag{2.3}$$

including both the viscous drag and the form drag (see e.g. Krogstad *et al.* 2005), simulated here by the roughness forcing term.

The last term on the right-hand side of (2.1) is the roughness forcing term. The form $\sim(-u_i|u_i|)$ ensures that the roughness forcing term always has a damping effect. The other parts of the roughness force term will be discussed in the following.

2.1. *Roughness factor*

The factor α_i will be referred to as the 'roughness factor' in the following and has the dimension of a line density $[\mathrm{L}^{-1}]$. In the limit of sparse roughness, this can be thought of as representing the density of the roughness elements. Sparse roughnesses would have a low α_i whereas less sparse roughnesses would correspond to a higher α_i. However, in the case of high α values, the analogy with the spacing of the roughness elements should be taken with caution. Although the roughness function ΔU^+ of a surface increases for sparsely spaced roughnesses with increasing solidity, it decreases once a sufficiently dense spacing of the roughness elements is reached due to shielding effects (Jiménez 2004). In the results presented later, shielding effects for high α values can be observed in some cases; in other cases the roughness continues to increase with high α depending on the shape function used (see § 4.3).

In addition to a line density, α could also be seen as a factor proportional to the overall drag coefficient of a roughness element and therefore no definite upper limit on α (such as 'densest spacing') can be given for the roughness factor.

2.2. *The roughness shape function and roughness height parameter*

The function $F_i(z, h_i)$ is the roughness shape function. The shape function regulates the influence of the roughness force term with respect to the distance from the wall z. The roughness height h_i parametrizes the extension of the roughness term into the flow. As will be shown in the following, there is no explicit relationship between the roughness height parameter and the actual physical height of a roughness element or its equivalent sand grain roughness, but the roughness height parameter is expected to increase with the physical roughness height.

We expect different types of roughnesses to correspond to different shape functions. As there is no straightforward mapping between a roughness element and its shape

function, we can only define some general conditions for $F_i(z, h_i)$. The roughness shape function should be bounded; far away from the wall the direct influence of the roughness term should vanish ($F_i(z, h_i) \to 0$ for $z \gg 0$); and the shape function should be greater than or equal to zero everywhere in order to ensure that the roughness term always has a damping effect.

In the following the definitions for the six shape functions used in this paper are given. In order to achieve a simple description, an auxiliary parameter $\eta(h)$ is used. The relationship between this auxiliary parameter and the roughness height parameter will be explained in the next paragraph. The first three shape functions are based on polynomials such as a simple box profile

$$F(z, h) = \begin{cases} 1 & \text{if } z \leqslant \eta(h), \\ 0 & \text{if } z > \eta(h), \end{cases} \tag{2.4}$$

a triangular profile

$$F(z, h) = \begin{cases} 1 - \dfrac{z}{\eta(h)} & \text{if } z \leqslant \eta(h), \\ 0 & \text{if } z > \eta(h), \end{cases} \tag{2.5}$$

and a parabolic profile

$$F(z, h) = \begin{cases} \left(1 - \dfrac{z}{\eta(h)}\right)^2 & \text{if } z \leqslant \eta(h), \\ 0 & \text{if } z > \eta(h). \end{cases} \tag{2.6}$$

The other three shape functions contain an exponential term and include an exponentially decaying profile

$$F(z, h) = \exp\left(-\frac{z}{\eta(h)}\right), \tag{2.7}$$

a Gaussian profile

$$F(z, h) = \exp\left(-\frac{z^2}{\eta(h)^2}\right) \tag{2.8}$$

and an 'orbital' profile

$$F(z, h) = \exp\left[2\left(1 - \frac{z}{\eta(h)}\right)\right] \frac{z^2}{\eta(h)^2} \tag{2.9}$$

(see illustrations in figure 1). The choice of the shape functions used in this article has been motivated not by a particular roughness but by their different mathematical properties. The first three shape functions are all discontinuous to some extent, either being discontinuous in themselves, such as the box profile, or in their first derivative (triangular profile) or second derivative (parabolic profile). The remaining three profiles are infinitely differentiable. The Gaussian profile can be thought of as a smeared-out box profile; the orbital profile distinguishes itself by being the only profile considered here that vanishes on the wall. Of all shape functions considered here, the exponentially decaying shape function extends (for a given roughness height) furthest into the flow, giving the highest value at the centreline of the channel. The fact that the exponentially decaying, Gaussian and orbital profiles extend infinitely into

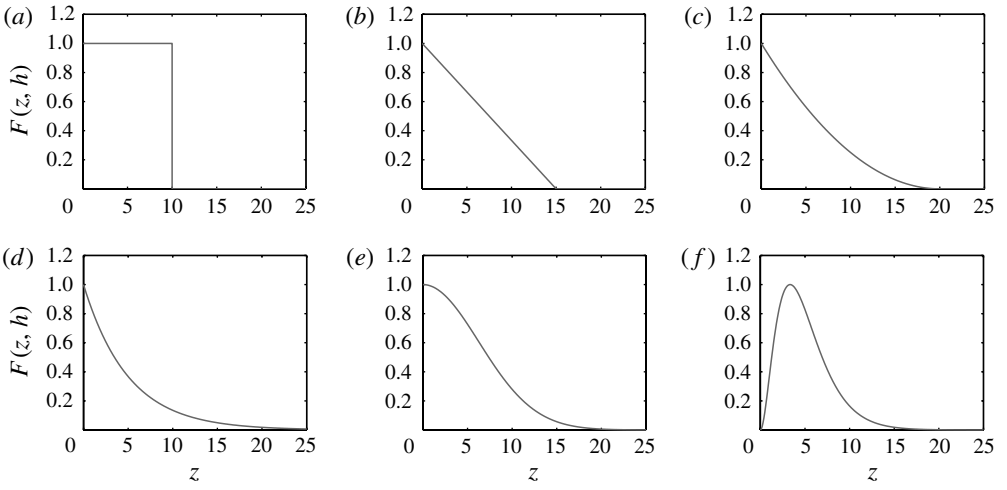

FIGURE 1. Different types of shape functions used to simulate roughnesses in this paper: (*a*) box; (*b*) triangular; (*c*) parabolic; (*d*) exponential; (*e*) Gaussian; and (*f*) orbital shape function. All shape functions are based on the same roughness height parameter $h = 5$.

the flow and have no clear vanishing point might not agree with the perception of a physical roughness element, which has a well-defined and finite height. However, the roughness element might not only affect the flow in its immediate surroundings but also change the flow further away from the wall. Furthermore, random roughness elements can give a wide range of height values (see e.g. Langelandsvik *et al.* 2008; Birch & Morrison 2011) better described by a distribution of roughness heights.

In order to make the effects of different shape functions and different roughness height parameters comparable, a clear definition for the roughness height of a profile and a rule for the normalization of the shape function are needed. In the case of the polynomial-based functions (2.4)–(2.6), the roughness height could be simply defined as the point $\eta(h)$ where the profile vanishes. However, this criterion could not be applied to the second group of profiles containing exponential functions (2.7)–(2.9). We therefore define the roughness height as the mean height of the profile as

$$h = \frac{\displaystyle\int_0^\infty F(z,h) z \,\mathrm{d}z}{\displaystyle\int_0^\infty F(z,h)\,\mathrm{d}z} \tag{2.10}$$

for a boundary layer or as

$$h = \frac{\displaystyle\int_0^\delta F(z,h) z \,\mathrm{d}z}{\displaystyle\int_0^\delta F(z,h)\,\mathrm{d}z} \tag{2.11}$$

for a channel flow, where δ is the channel half-height. This definition should work for all reasonable roughness functions, which obey the general criteria given above. Note that this definition of the roughness height does not correspond to the tops of the shape function for the polynomial-based roughness functions, e.g. for the box

profile $\eta(h) = 2h$. In some cases the auxiliary parameter $\eta(h)$ has to be found by solving an integral equation.

In addition, a rule for the normalization of the roughness function is needed to enable a comparison of the roughness factor effects for different roughness heights and different shape functions. The roughness functions are normalized by setting their maxima to unity,

$$\max(F(z, h)) = 1. \tag{2.12}$$

Another possible normalization can be based on the integral of the roughness shape function. The definition (2.12) has been chosen as it facilitates the interpretation of the roughness factor α in the terms of the spacing of the roughness elements.

The concept of the shape function used here has been influenced by an approach in discrete element methods where a local drag coefficient is used to express the form drag force caused by roughness elements penetrating the control volume (Taylor *et al.* 1985) and also bears some resemblance to porosity profiles used in the volume-averaged Navier–Stokes equations for the modelling of flows over porous surfaces (Breugem & Boersma 2005).

2.3. *The form of the roughness term*

The term was chosen quadratic in the respective velocity component in order to model form drag effects, since an object moving in a high-Reynolds-number flow experiences a quadratic drag force of the form $\sim -|\boldsymbol{u}|u_i$ (see e.g. Batchelor 1967). However, roughness elements on a wall show only limited resemblance to an object in a free stream velocity field at high Reynolds number. Using the full form of the quadratic drag term $\sim -|\boldsymbol{u}|u_i$ instead of the choice $\sim -|u_i|u_i$ leads to a stronger damping of the spanwise and wall-normal velocity fluctuations and impairs the outer-layer similarity of the mean streamwise velocity profile.

Besides creating extra form drag, rough walls are also known to influence the viscous generation cycle (Jiménez 2004) and can even reduce the skin friction, most notably in the case of riblet surfaces (Bechert *et al.* 1997). The roughness force term does not explicitly try to model changes in the viscous effects of the boundary. It is to some extent possible to model a weakening of the skin friction by adjusting the relative strengths of the streamwise and spanwise components of the roughness term (see § 4.1).

It should be noted that the roughness term is only intended for the simulation of k-type roughnesses and that we do not try to match the special effects of d-type roughnesses. As d-type roughnesses occur under very specific circumstances, this does not significantly impair the general applicability of the model.

3. Numerical method

In order to explore the effects of the roughness force term on turbulent channel flow, a large number of direct numerical simulations (DNSs) were conducted. The Navier–Stokes equations were solved by a standard second-order finite-difference method on a staggered grid. A second-order Adams–Bashforth method was employed for the time advancement. The presence of the roughness term did not compromise the stability of the scheme due to its damping character.

The simulations were conducted for a Reynolds number of $Re_\tau = 180$ using a box of size $7 \times 3.5 \times 2$ and a grid of size $128 \times 128 \times 128$, where x is the streamwise, y the spanwise and z the wall-normal direction. The grid is equidistantly spaced in the

streamwise and spanwise directions and stretched in the wall-normal direction to give a higher resolution near the walls ($\Delta z^+_{min} = 0.75$ and $\Delta z^+_{max} = 4.9$). Standard no-slip boundary conditions are imposed on the lower and upper walls of the channel. The flow is maintained by a constant mean streamwise pressure gradient.

The roughness term is in all cases applied symmetrically to the upper and lower parts of the channel, with the shape function being symmetric to the centreline of the channel. This simplifies the interpretation of the results, as no further anisotropy effects need to be taken into account.

4. Results

In its proposed form, the roughness force term is very flexible: the roughness factor and roughness height parameter can be varied and different shape functions can be chosen. One could use a different shape function and different values of the roughness factor for each component of the roughness force term. In order to limit the number of cases to study, the effects of the different components of the roughness force term were first considered. The streamwise–spanwise combination (see below) was chosen for the main parameter study, where the roughness height and factor were varied systematically and different shape functions were employed.

4.1. *The effect of the components of the roughness force term*

The effect of the components of the roughness force term is considered for a configuration that uses a Gaussian shape function with a roughness height of $h^+ = 10$. The roughness factor α_i is set either to 0 or 1, which gives eight possible combinations including the smooth-wall case (see table 1). The focus in this section is on the mean streamwise velocity profile (shown in figure 2). The values for the downwards shift in the velocity profile – the roughness function ΔU^+ (see introduction) – have been estimated by subtracting the mean centreline velocity $U_c = \langle u(\delta) \rangle$ from the centreline velocity in the reference case (a smooth-wall channel flow),

$$\Delta U^+ = U_c^{ref} - U_c. \tag{4.1}$$

As no well-developed log law can be observed at Reynolds number $Re_\tau = 180$ (Moser, Kim & Mansour 1999; Hu, Morfey & Sandham 2006), the usual manner for the estimation of the roughness function by fitting a log law is sensitive to the choice of the fitting parameters; therefore the estimate based on the centreline velocity has been chosen. Since a good preservation of the outer scaling of the mean streamwise velocity profile is observed in most cases (see § 4.4), the estimate based on the centreline velocity should not be adversely affected by the wake component.

In all cases where the streamwise roughness term is present, a clear downwards shift can be observed in the velocity profile. The effects of the other two terms are far weaker; there is little difference in the mean streamwise velocity profile for cases 1, 2, 5 and 7. The spanwise and wall-normal roughness terms both have a weak drag-reducing effect: a small upwards shift can be observed in the cases without a streamwise roughness term, and in combination with a streamwise roughness term (cases 1, 5 and 7) the drag increase is less than in case 2 (purely streamwise roughness). Of the wall-normal and spanwise roughness terms, the latter has the stronger effects on the mean velocity profile. This is probably a result of the higher level of fluctuations observed for the spanwise velocity compared to the wall-normal velocity in the near-wall region. The drag-reducing effects of the wall-normal forcing term are consistent with the observations of Orlandi *et al.* (2003), who

Case	Legend	α_x	α_y	α_z	ΔU^+
1	xyz	1.0	1.0	1.0	7.9
2	x	1.0	0	0	8.3
3	y	0	1.0	0	−0.5
4	z	0	0	1.0	−0.1
5	xy	1.0	1.0	0	8.0
6	yz	0	1.0	1.0	−0.5
7	xz	1.0	0	1.0	8.2
8	Smooth	0	0	0	0

TABLE 1. Different combinations of the roughness term and measured values for the roughness function ΔU^+. A Gaussian shape function and a roughness height of $h^+ = 10$ have been used.

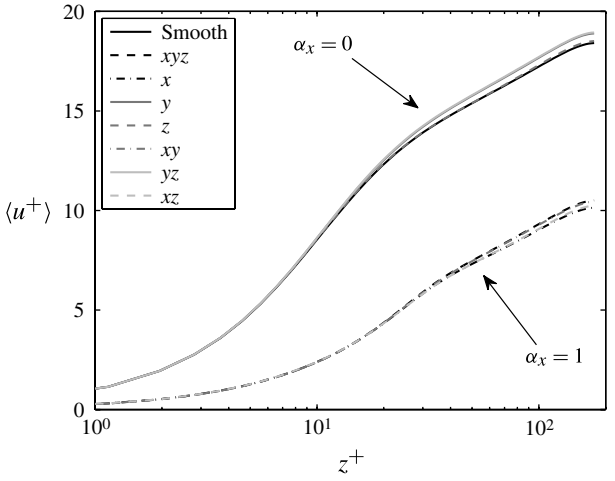

FIGURE 2. Mean streamwise velocity profile for different roughness factor α_i combinations in the roughness force term. A Gaussian shape function has been used. The legend refers to the second column of table 1. The lower group of curves consists of cases including the streamwise component of the roughness term ($\alpha_x = 1$), whereas for the upper group of curves $\alpha_x = 0$.

found a drag increase when wall-normal velocity disturbances were applied at the wall. However, Orlandi *et al.* found only a very small effect for spanwise velocity fluctuations. This could be related to the fact that their data were for a spanwise bar case.

As it is difficult to interpret the roughness term for the wall-normal component (unless one considers overhanging roughness elements), and this term has the weakest effect and an adverse effect on the outer-layer scaling of the flow (not shown), we will concentrate in the following on the streamwise and spanwise roughness terms, setting the wall-normal roughness factor to zero in all cases. Purely spanwise roughnesses, or a combination where $\alpha_2 \gg \alpha_1$, could potentially be used for the simulation of flow over riblet surfaces, where a drag-reducing effect is observed for a limited range of Reynolds numbers (Bechert *et al.* 1997; Karniadakis & Choi 2003).

4.2. *Parameter range in main parameter study*

In the main parameter study, the same shape functions and roughness factors $\alpha_x = \alpha_y = \alpha$ have been used for the streamwise and spanwise roughness terms; the wall-normal roughness term has been set to zero. Most cases of the study were run either for the box or the Gaussian shape function. The roughness factor has been varied over several orders of magnitude $\alpha = 0.04,\ 0.1,\ 0.4,\ 1,\ 4,\ 10$, whereas the roughness height parameter was more constrained due to the low Reynolds number $Re_\tau = 180$ at which the simulations were conducted ($h^+ = 2.5,\ 5,\ 7.5,\ 10,\ 15,\ 20,\ 25,\ 30$), resulting in 48 simulations per shape function. For the remaining four profiles introduced in § 2.2, the triangular, parabolic, exponentially decaying and orbital profiles, only one roughness factor $\alpha = 1$ has been studied for the same range of roughness heights.

4.3. *The roughness function*

The dependence of the roughness function ΔU^+ on the roughness height parameter h^+ and roughness factor α is shown in figures 3(*a*) and 4. As can be observed from figure 3(*a*), the roughness function ΔU^+ rises with increasing values of the roughness height parameter h^+. This is the expected and desired result, as the effect of the roughness force term extends further towards the middle of the channel and should correspond to a higher roughness element. With increasing roughness factor α, the roughness function ΔU^+ in general also increases. This is in line with the conception of the roughness term, as one would usually expect a stronger effect for more densely spaced roughness elements or for roughness elements with a higher drag coefficient. For $\alpha = 1$, where we have data for all shape functions discussed in this paper, the results for different shape functions do not vary strongly. However, at the lower and higher ends of the roughness factors studied, differences between the Gaussian and box profile are discernible. For the lower roughness factors, the box profile has the stronger effect, leading to higher values of ΔU^+, whereas for the highest two roughness factors $\alpha = 4$ and $\alpha = 10$ the values of ΔU^+ for the Gaussian shape function exceed the values for the box shape function. In the case of the box shape function, an effect that resembles the shielding phenomenon (mentioned in § 2.1) can be observed in figure 4. For the higher roughness heights ($h^+ = 15,\ 20,\ 25,\ 30$), ΔU^+ decreases from $\alpha = 4$ to $\alpha = 10$. A possible explanation for this behaviour could be that the roughness force term using the box profile is in these cases so strong as to damp virtually the entire streamwise momentum near the wall and results effectively in an offset of the wall to $z = 2h$.

A further observation can be made from figure 4. A rapid increase in ΔU^+ from $h^+ = 2.5$ to $h^+ = 5$ can be observed when going for a fixed value α (e.g. $\alpha = 1$) in the vertical direction of the figure. For higher roughness heights, the increase is more gradual. This behaviour puts one in mind of the question of the existence of a 'critical roughness height' that has to be exceeded in order to observe roughness effects and is conventionally set at $k_s^+ \approx 5$ (Nikuradse 1950; Schlichting 1968) but has been debated in recent years (Bradshaw 2000; Jiménez 2004). The threshold-like behaviour observed when going from $h^+ = 2.5$ to $h^+ = 5$ could be reconciled with the concept of a 'critical roughness height' but, as the threshold-like behaviour still shows a finite slope, there is no definite evidence for this.

Returning to the dependence of the roughness function on the height parameter h^+ (see figure 3), it is obvious that the curves $\Delta U^+_{F,\alpha}(h^+)$ for different roughness factors and shape functions all have approximately the same shape in the region $3 \leqslant \Delta U^+ \leqslant 10$. Within this range, all curves can be collapsed onto the logarithmic

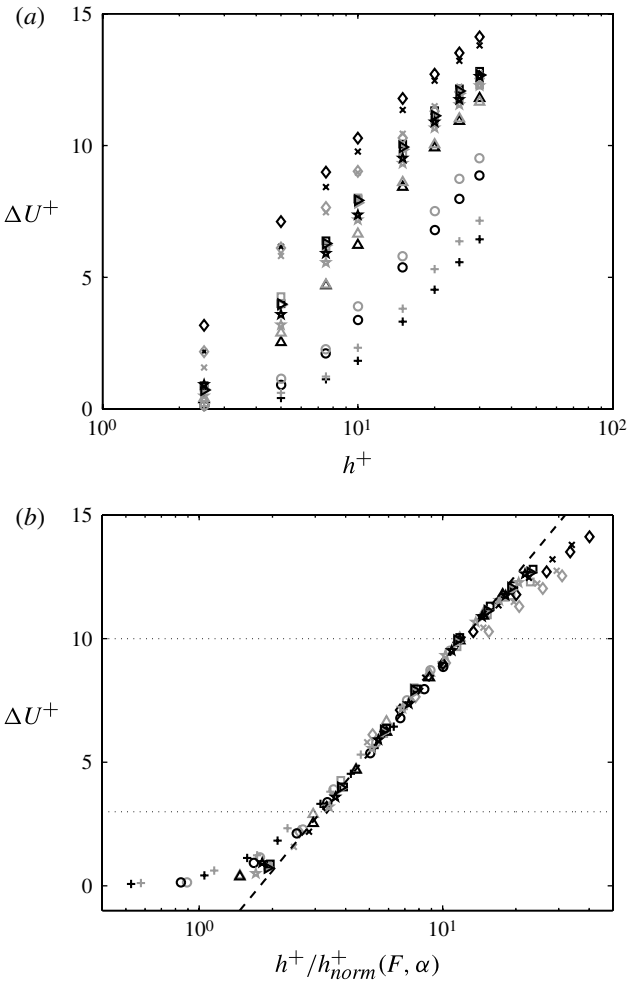

FIGURE 3. (*a*) Roughness function for different roughness factors and shape functions plotted versus roughness height parameter: for the Gaussian profile (black symbols) and box profile (grey symbols) results are shown for six different roughness factors (+, $\alpha = 0.04$; ○, $\alpha = 0.1$; △, $\alpha = 0.4$; □, $\alpha = 1$; ×, $\alpha = 4$; ◇, $\alpha = 10$) and different shape functions. For the four remaining shape functions, results are shown for $\alpha = 1$: triangular profile (black ▷), parabolic profile (grey ▷), exponentially decaying profile (black ⋆) and orbital profile (grey ⋆). (*b*) Roughness function plotted versus rescaled height parameter; legend for symbols as in panel (*a*). The dashed line shows the best fit (see (4.2)) in the interval $3 \leqslant \Delta U^+ \leqslant 10$.

expression

$$\Delta U^+(h^+/h^+_{norm}) = 5.2\ln(h^+/h^+_{norm}) - 3 \tag{4.2}$$

by rescaling the height values by a fitting factor h^+_{norm} dependent on the shape function and the roughness factor α, i.e. $h^+_{norm} = h^+_{norm}(F, \alpha)$. The collapse is not satisfactory for values outside this range ($\Delta U^+ < 3$ and $\Delta U^+ > 10$). For low ΔU^+, the curves for low values of α show a more gradual increase in the transitionally rough region than the curves at higher α. As the behaviour in the transitionally rough region depends on the type of rough surface, the spread for low ΔU^+ is not unexpected. For the

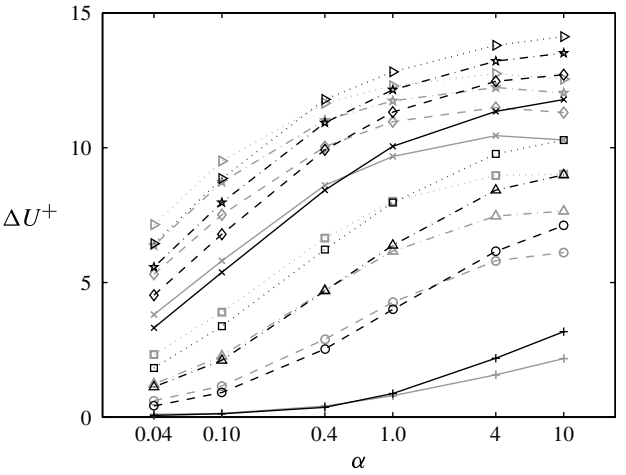

FIGURE 4. Roughness function plotted versus roughness factor for different values of the roughness height parameter (+, $h^+ = 2.5$; ○, $h^+ = 5$; △, $h^+ = 7.5$; □, $h^+ = 10$; ×, $h^+ = 15$; ◇, $h^+ = 20$; ⋆, $h^+ = 25$; ▷, $h^+ = 30$). The black symbols/lines are for the Gaussian shape function; grey symbols/lines are for the box shape function.

points that deviate for $\Delta U^+ > 10$, several reasons for the departure can be given. In the case of the box profile, we already observed shielding-like saturation effects for high roughness factors. These account for the strong departure from the fit for $\Delta U^+ > 10$. In the other cases the (less-pronounced) departure from the fitted curve can be attributed to the low Reynolds number used here. Owing to the small height of the channel measured in friction length scales, outer similarity cannot be recovered once high values of the roughness function are reached (see also the following subsection). Furthermore it should be noted that in most experiments (conducted at far higher Reynolds numbers) the measured values for the roughness function do not exceed $\Delta U^+ \approx 11$. Therefore the cases with $\Delta U^+ > 10$ will be classified as 'extremely rough' in the following. The good collapse of the curves up to $\Delta U^+ = 10$ suggests that the Reynolds number Re_τ used in this parameter study is sufficiently high to establish the overall effects of the roughness term.

A comparison of the dependence of the roughness function on the (rescaled) height parameter (see figure 3*b*) with the dependence of typical experimental values of the roughness function on the equivalent sand grain roughness (Jiménez 2004) shows that the curve for the height parameter has a different slope in the fully rough regime. This can also be inferred from the prefactor 5.2 in front of the logarithmic term in the curve fitted to the data (see (4.2)). Therefore the height parameter is not a linear function of the equivalent sand grain roughness. A correspondence with equivalent sand grain roughness size can be recovered in the fully rough region by taking the rescaled roughness height raised to a power of γ. The value of γ depends on the region where the results are fitted to the asymptotic behaviour for the fully rough region:

$$\Delta U^+(k_s^+) = \kappa^{-1} \ln(k_s^+) + A - 8.5. \tag{4.3}$$

The most obvious region for the fit would be the region $3 \leqslant \Delta U^+ \leqslant 10$ where we have already observed a logarithmic behaviour giving an exponent $\gamma \approx 2.08$ (see figure 5*a*). Conventionally, the equivalent sand grain roughness is estimated using the data in the

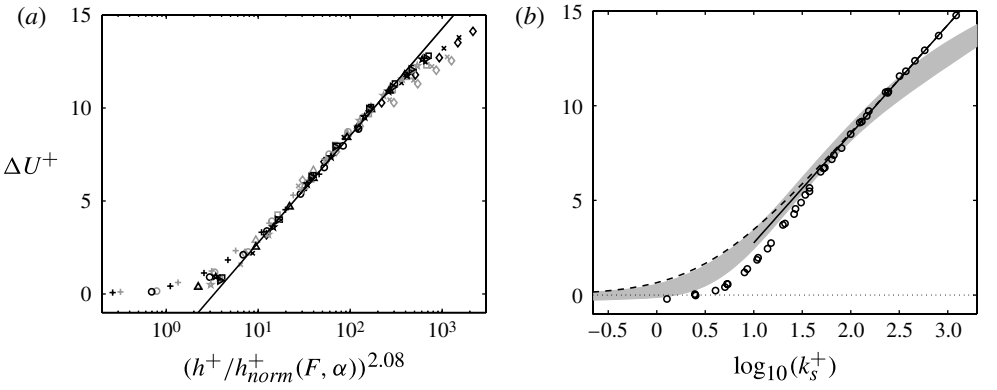

FIGURE 5. (*a*) Roughness function for different roughness factors and different shape functions plotted versus normalized and exponentiated roughness height parameter (symbols as in figure 3). The black line shows the fully rough asymptote. (*b*) Comparison of rescaled roughness data (shaded region) with the Nikuradse (1950) sand grain roughness data (black circles) and the Colebrook interpolation formula (4.4) (dashed black line). The fully rough asymptote is shown by the continuous black line.

fully rough region only; if we use $7 \leqslant \Delta U^+ \leqslant 10$ (the higher values of the roughness function $\Delta U^+ > 10$ are discarded for the reasons given above) for the fit, a lower value for the exponent γ results ($\gamma \approx 1.88$).

In figure 5(*b*) the rescaled roughness data are compared to the data of Nikuradse (1950) for his sand grain experiments and the Colebrook interpolation formula (Jiménez 2004)

$$\Delta U^+(k_s^+) = \kappa^{-1} \ln(0.3k_s^+ + 1), \tag{4.4}$$

which applies to industrial steel pipes. The envelope of the rescaled roughness data just touches the Colebrook curve but is slightly above Nikuradse's data. The exact location of the envelope depends on the rescaling exponent γ. In figure 5 $\gamma = 2.08$ has been used; for the lower exponent $\gamma = 1.88$, the envelope would approach Nikuradse's data more closely. For the extremely rough cases $\Delta U^+ > 11$ the envelope to our data falls below the fully rough asymptote for the reasons mentioned above.

To conclude this section, it should be noted that these numerical simulations differ from standard experiments in the way the curve for a given roughness (roughness factor and shape function) is obtained. In an experiment the roughness function is usually measured for different equivalent sand grain roughnesses by varying the Reynolds number of the flow; the physical size of the roughness in absolute (outer) units remains constant. In our case the extension of the roughness term into the flow is varied for a constant Reynolds number Re_τ that is significantly lower than the Reynolds numbers of typical experiments. A related issue is that the equivalent sand grain roughness k_s^+ exceeds the actual height of the channel for the highest values of the height parameter h^+ (see figure 5). This can be explained by keeping in mind that sand grain roughness is not the most efficient of roughnesses and that k_s^+ can be used interchangeably with the roughness function ΔU^+ in the fully rough case. For moderate Reynolds numbers the $\Delta U^+(k_s^+ = \delta^+)$ is not very high. The high values attained for the equivalent sand grain roughness therefore merely indicate that extremely rough surfaces can be modelled by the roughness force term.

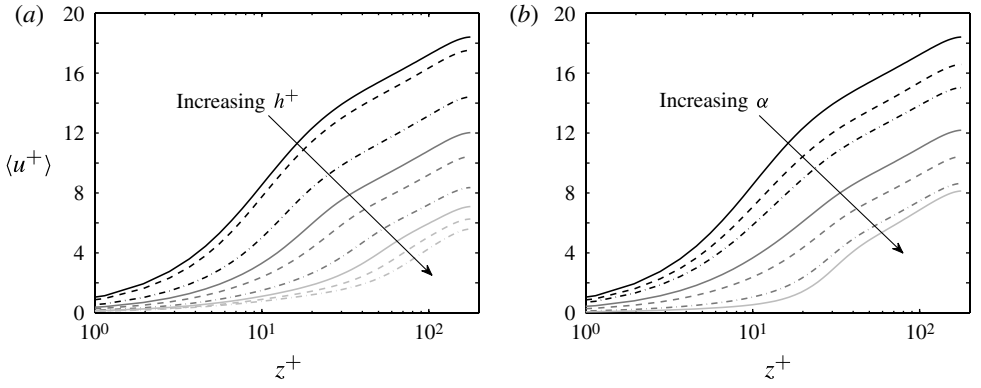

FIGURE 6. Mean streamwise velocity profile across the channel using a Gaussian shape function. (*a*) Constant roughness factor $\alpha = 1.0$ and varying roughness height ($h^+ = 2.5$, 5, 7.5, 10, 15, 20, 25 and 30). (*b*) Varying roughness factor ($\alpha = 0.04$, 0.1, 0.4, 1, 4 and 10) and constant roughness height parameter $h^+ = 10$. The continuous black line corresponds to the smooth-wall reference case.

4.4. *Mean streamwise velocity profile*

In this section the effects of the roughness height and roughness factor on the mean streamwise velocity profile and the velocity defect profile are discussed. A closer look is taken at the influence of the shape function using the first and second wall-normal derivative of the mean streamwise velocity profile.

4.4.1. *The influence of the roughness height and the roughness factor*

The influence of the roughness height and the roughness factor show the same trends for all shape functions studied so far and will be illustrated here using the Gaussian shape function. With increasing roughness height, the changes in the velocity profile extend increasingly towards the middle of the channel, resulting in a lower centreline velocity (see figure 6). Similar observations were made in numerical simulations where the height of the roughness elements was varied systematically (DeMarchis, Napoli & Armenio 2010). The effect of increasing the roughness factor compared to increasing h^+ is mainly an increased reduction of the near-wall velocity. The different effects of α and h^+ on the mean streamwise velocity profile become clearer when one compares two cases with different (α, h^+) combinations that give a similar value for ΔU^+, e.g. cases ($\alpha = 10,\ h^+ = 10$) and ($\alpha = 1,\ h^+ = 15$) shown in figure 6. In the case of the higher roughness height ($\alpha = 1,\ h^+ = 15$), the effect of the roughness force term is distributed over a larger part of the profile, whereas in the case of the higher roughness factor ($\alpha = 10,\ h^+ = 10$), the effect of the roughness force term is concentrated near the wall, leading to a very small streamwise velocity near the wall and a steeper increase for $z^+ \gtrapprox 2h^+$.

Almost all the roughness height and factor combinations studied here result in the same velocity defect profile in the outer layer, agreeing with the result for the smooth-wall reference case (see figure 7). The outer similarity is lost only for combinations corresponding to very high values of the roughness function. This behaviour is in line with the expected behaviour for rough surfaces, where universality for the mean flow in the outer layer is expected for all but extremely rough surfaces (Jiménez 2004; Castro 2007; Schultz & Flack 2009). For increasing roughness height, the departure

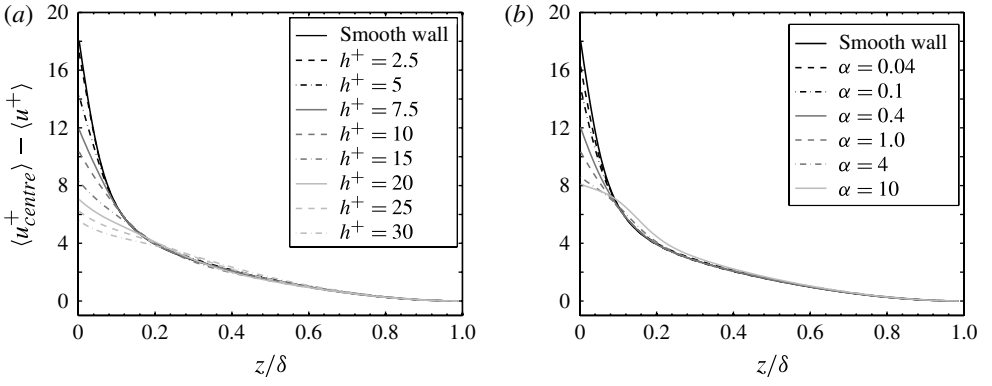

FIGURE 7. Velocity defect profile across the channel using a Gaussian shape function. (*a*) Constant roughness factor $\alpha = 1.0$ and varying roughness height. (*b*) Varying roughness factor and constant roughness height parameter $h^+ = 10$.

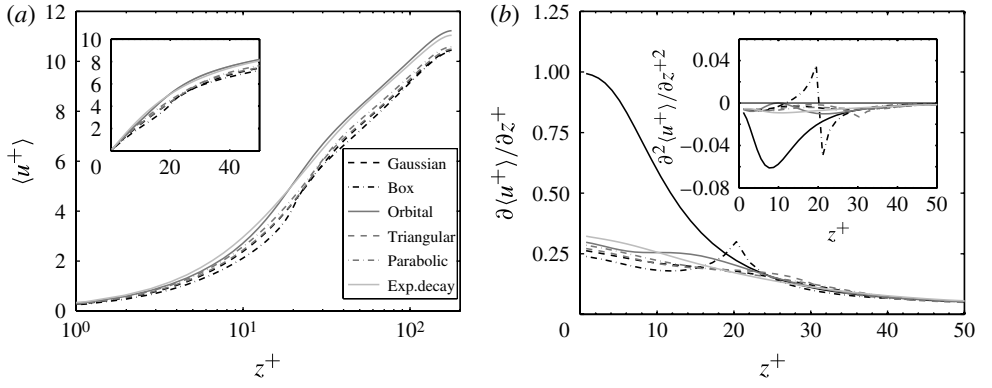

FIGURE 8. (*a*) Mean streamwise velocity profile across the channel for different shape functions (inset in linear scales). (*b*) First and second (inset) derivatives of mean streamwise velocity profile. The roughness factor is $\alpha = 1$, roughness height parameter $h^+ = 10$. The legend of panel (*a*) applies also to (*b*). The continuous black line in panel (*b*) shows the smooth-wall reference case.

from the reference case occurs for greater distances from the wall. There is also a weaker trend towards an earlier departure for increasing roughness factors.

4.4.2. *The influence of the roughness shape function*

As has already been observed in § 4.3, the shape function has some influence on the value of the roughness function. This difference is most noticeable for very small or very high roughness factors. The shape of the streamwise velocity profile does not vary dramatically for different shape functions (see figure 8). The differences induced by the shape function show up more clearly in the first and especially the second derivative of the mean streamwise velocity profile with respect to the wall-normal coordinate. In the cases shown in figure 8 these differences are confined to the region near the wall ($z^+ < 40$). Towards the middle of the channel the first and second derivatives collapse onto the corresponding curves for the smooth-wall reference case.

The most distinct feature in the near-wall region is the pronounced inflection point that can be observed for the box shape function. The inflection point coincides with the top of the box shape function (at $z^+ \approx 2h^+ = 20$ for the example shown in figure 8), which is also the point where the box shape function is discontinuous. For the triangular profile a small peak can be observed in the second derivative, which is located at the top of this profile ($z^+ = 30$ for the case shown in figure 8), but no remarkable features show up in the first derivative of the mean streamwise velocity profile for this shape function. Discontinuities in the shape function or in its derivatives therefore have consequences for the mean streamwise velocity profile; however, it seems to be a sufficient condition for a smooth velocity profile that the shape function is twice differentiable, as we observe no remarkable features for the results using the parabolic shape function. For all shape functions, a good outer-layer similarity is preserved in moderately rough cases. In extremely rough cases the outer-layer similarity is lost, as discussed for the Gaussian shape function above.

Inflection points in the mean streamwise velocity profile can lead to Kelvin–Helmholtz instabilities that influence the large-scale structure dynamics of the turbulence. In a smooth-wall channel flow, no inflection points are present in the time-averaged mean streamwise velocity profile. The roughness term sometimes introduces an inflection point into the profile. For the box profile, in almost all cases studied here, an inflection point can be found in the mean streamwise velocity profile. The exceptions occur only for small roughnesses $\Delta U^+ < 2.5$. For the box profile these inflection points occur at $z \approx 2h$, i.e. approximately at the top of the shape function. For the Gaussian shape function, inflection points occur for high values of the roughness factor ($\alpha = 4, 10$) and for the higher roughness heights ($h^+ = 20,\ 25,\ 30$) in the case $\alpha = 1$. These inflection points are found further away from the wall at $z \approx 2.5h$ and are typically much less pronounced than those for the box shape function. For the orbital and triangular shape functions, some weak inflection points can also be found. No inflection points have been observed in cases using the parabolic or the exponentially decaying shape function.

It is difficult to compare these observations to experimental results, as measurements near the wall are complicated by the presence of the rough surface. Most studies (including numerical studies) show the profiles only above the roughness elements and not within the roughness layer. The spatially averaged mean streamwise velocity profiles shown in, for example, Xie, Coceal & Castro (2008) and Chan-Braun, Garcia-Villalba & Uhlmann (2011) suggest that in most cases the profiles will tend to follow curves comparable to the smoother mean streamwise velocity profiles obtained here using the Gaussian or parabolic shape functions. However, the results for the box shape function put one in mind of a characteristic feature of flow over plant canopies: the presence of a strong inflection point in the mean streamwise velocity profile that is located at the height of the canopies (Finnigan 2000). The box shape function might therefore be a good choice for an attempt to model a plant canopy by the roughness term. However, inflection points in the velocity profile are not confined to plant canopies; they also occur for many other types of rough surfaces (Castro 2009).

4.5. *Reynolds stresses*

Rough walls are known not only to change the mean velocity profile but also to influence the level of turbulent fluctuations. In this section the effect of the roughness force term on the velocity fluctuations is studied using the profiles of the mean Reynolds stresses across the channel. By computing the anisotropy invariant map of

the Reynolds stresses, a first insight is gained into the changes of the structure of the turbulent flow caused by the roughness term.

4.5.1. *Influence of roughness height and factor parameters*

The effects of the roughness height h^+ and roughness factor α on the turbulent velocity fluctuations are best observed for the streamwise normal stresses and the shear stress (see figure 9*a*,*b*,*g*,*h*). With increasing roughness height, the near-wall peaks in $\langle u^2 \rangle$ and $-\langle uw \rangle$ are reduced and they move further away from the wall. The peak is flattened with increasing roughness height. An increasing roughness factor also induces a relocation of the peaks towards the middle of the channel, but its main effect is to damp the near-wall fluctuations. In the outer region, the curves collapse with the reference case. The collapse onto the smooth-wall reference curve is delayed to higher distances from the wall for higher roughness heights as observed for the mean streamwise velocity profile.

A similar reduction in the peak values of the streamwise normal stress as well as the shear stress has been observed in many experiments (see e.g. Krogstad *et al.* (2005) and references therein). The collapse in the outer layer for the profile of the streamwise velocity fluctuations is also in agreement with experimental observations and DNSs, where such a collapse has been found (Bakken *et al.* 2005; Leonardi & Castro 2010; Amir & Castro 2011).

The results for the spanwise and wall-normal stresses (see figure 9*c*–*f*) are less conclusive. In general, the roughness factor has a much lower influence on the level of spanwise and wall-normal velocity fluctuations than the roughness height parameter. For small roughness heights and small to moderate values of the roughness factor, the level of fluctuations is little changed compared to the reference case. This is in agreement with the expected behaviour for rough-wall channel flow, as the levels of the wall-normal and spanwise stresses are usually of similar magnitude to those in the smooth-wall case (Bakken *et al.* 2005; Krogstad *et al.* 2005; Amir & Castro 2011). However, for high roughness heights and high values of the roughness factor, the wall-normal and spanwise velocity fluctuations are strongly reduced and their peaks move towards the middle of the channel. This behaviour can largely be attributed to a low-Reynolds-number effect. It gets weaker with increasing Reynolds number as the peaks of the streamwise and wall-normal velocity fluctuations move (in inner units) further away from the wall (see e.g. Hu *et al.* 2006) and thus further away from the direct action of the roughness term. In the example shown in § 5, performed at $Re_\tau = 400$, the level of the spanwise and wall-normal fluctuations is captured well by the roughness term. It is also beneficial to employ a shape function that does not extend very far into the flow, e.g. the box shape function gives much better results for the same h^+ than the exponentially decaying shape function (see following subsection). For very high roughnesses, the roughness term will probably lead to an overdamping of the spanwise and wall-normal fluctuations even at higher Reynolds numbers. This can be attributed to the purely damping nature of the roughness forcing term. One might suspect that the spanwise roughness term is responsible for the overdamping of $\langle v^2 \rangle$ and $\langle w^2 \rangle$. However, similar levels of $\langle v^2 \rangle$ and $\langle w^2 \rangle$ are observed for the x, xy, xz and xyz combinations studied in § 4.1.

It is obvious from the plot for the Reynolds shear stress, but also clearly visible in the normal stress components, that an increase of the roughness factor results in a smaller reduction in the Reynolds stresses than does an increase in the roughness height. This is also observed if one compares different (α, h) combinations that give the same value of ΔU^+ (not shown). A possible explanation for this behaviour is

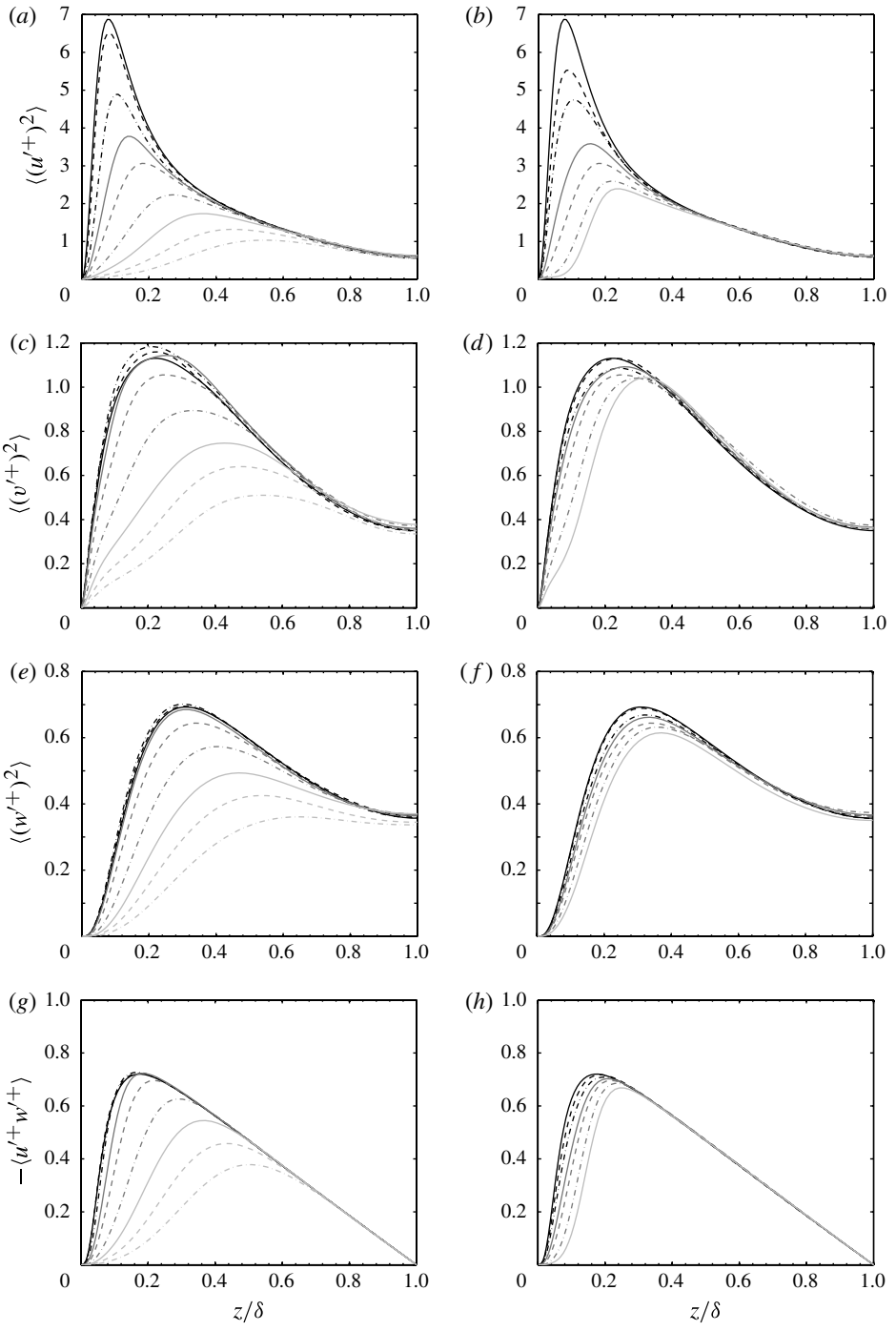

FIGURE 9. Profiles of Reynolds stresses across channel: (*a*,*b*) streamwise normal stress; (*c*,*d*) spanwise normal stress; (*e*,*f*) wall-normal stress; and (*g*,*h*) shear stress. (*a*,*c*,*e*,*g*) Constant roughness factor $\alpha = 1.0$ and varying roughness height ($h^+ = 2.5$, 5, 7.5, 10, 15, 20, 25 and 30); line styles as in figure 6(*a*). (*b*,*d*,*f*,*h*) Constant roughness height $h^+ = 10$ and varying roughness factor ($\alpha = 0.04$, 0.1, 0.4, 1, 4 and 10); line styles as in figure 6(*b*). In all cases a Gaussian shape function has been used.

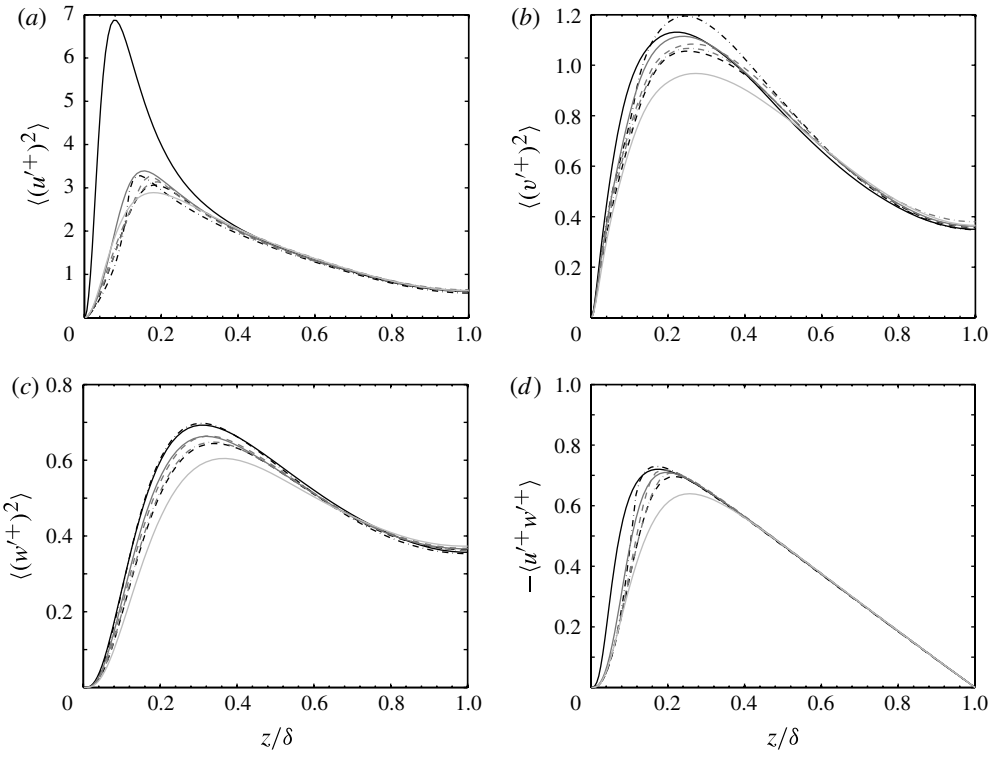

FIGURE 10. Profiles of Reynolds stresses for different shape functions using a roughness factor $\alpha = 1$ and height parameter $h^+ = 10$: (*a*) streamwise normal stress; (*b*) spanwise normal stress; (*c*) wall-normal stress; and (*d*) shear stress. Line styles as in figure 8.

that a (high α, low h) combination results in a mean streamwise velocity profile that has a much higher shear rate $\partial u/\partial z$ in the outer part of the rough region than a (low α, high h) combination that results in the same value of ΔU^+. The first combination is therefore more likely to sustain strong turbulent fluctuations than the latter.

4.5.2. *Effects of the roughness shape function*

The effect of the shape function on the profiles of the Reynolds stresses is more pronounced than the effect on the mean streamwise velocity profile (see figure 10). For the streamwise normal Reynolds stress, outer-layer similarity is preserved in all but extremely rough cases. Towards the middle of the channel, all the Reynolds shear stress curves collapse on the reference case. The velocity fluctuations are affected most strongly by the exponentially decaying shape function. For the Reynolds shear stress, the curve for the exponentially decaying shape function does not collapse onto the reference case up to a distance of $z/\delta \approx 0.4$ from the wall, whereas in all other cases a good collapse can be observed for $z/\delta > 0.25$. The peak values of the spanwise and wall-normal stresses for this shape function are considerably smaller than for the other shape functions. This behaviour may be due to the fact that the exponentially decaying shape function extends furthest into the flow of all the shape functions considered here. Therefore the direct action of the roughness force term extends further from the wall than for all other shape functions.

The curves for the box shape function also show some distinguishing features. The peak for the streamwise normal stress is characteristically skewed. This can be attributed to the fact that there is a sharp increase in the fluctuations above the top of the roughness shape function (which is located at $\approx 0.11\delta$ for $h^+ = 10$). The wall-normal velocity fluctuations have almost the same intensity as in the smooth-wall reference case, whereas they are reduced in all other cases. The outer-layer similarity is best preserved for the box shape function. This is probably a consequence of the fact that the direct effects of the box shape function are confined to a region close to the wall whereas all other shape functions extend further into the flow. The remaining shape functions do not introduce any extraordinary features in the profiles of the Reynolds stresses.

4.5.3. *Anisotropy of Reynolds stresses*

A standard measure for the anisotropy of the turbulent velocity fluctuations is the Reynolds stress anisotropy tensor. This is defined as

$$b_{ij} = \frac{\langle u_i' u_j' \rangle}{\langle u_\beta' u_\beta' \rangle} - \frac{1}{3}\delta_{ij}, \tag{4.5}$$

where δ_{ij} is the Kronecker delta and $\langle u_\beta' u_\beta' \rangle$ is twice the turbulent kinetic energy. The Reynolds stress anisotropy tensor is traceless and symmetric; its elements are bounded by $-1/3 \leqslant b_{ij} \leqslant 2/3$. In isotropic turbulence, all elements of this tensor vanish.

The anisotropy invariant map (Lumley 1978; Pope 2000; Simonsen & Krogstad 2005) provides a convenient overview of the anisotropy of the Reynolds stresses. It is constructed using the second and third principal invariants of the Reynolds stress anisotropy tensor defined as $\mathrm{II}_b = -\sum_{i,j} b_{ij} b_{ji}/2$ and $\mathrm{III}_b = \sum_{i,j,k} b_{ij} b_{jk} b_{ki}/3$. There are two ways to construct the anisotropy invariant map, (i) the original way as proposed by Lumley (1978), a cross-plot of $-\mathrm{II}_b$ versus III_b, or (ii) using the derived quantities ξ and η (where $\xi^3 = \mathrm{III}_b/2$ and $\eta^2 = -\mathrm{II}_b/3$), which give a less distorted triangle and are therefore preferred by some authors (Pope 2000). In both cases, the vertical axis corresponds to the degree of anisotropy whereas the horizontal axis indicates the type of the anisotropy. All possible turbulent states on the anisotropy invariant map are contained within the Lumley triangle (see figure 11). In terms of ξ and η, the left and right sides of the Lumley triangle are given by $\eta = \pm\xi$, where the left side corresponds to a disc-like turbulent state and the right side to rod-like turbulence. The upper side of the triangle is defined by $\eta = (1/27 + 2\xi^3)^{1/2}$ and corresponds to two-component turbulence. The lower apex of the triangle at $\xi = 0, \eta = 0$ indicates isotropic turbulence.

In a channel flow without roughness (as shown for the reference case in figure 11), the turbulence is of two-component type close to the wall, following the upper boundary of the Lumley triangle, as the wall-normal velocity fluctuations are much weaker than the streamwise and spanwise ones. The anisotropy increases while traversing the viscous sublayer, reaching its peak value at $z^+ \approx 8$. Further away from the wall, the wall-normal fluctuations gain in strength and the turbulence is now close to a rod-like axisymmetric state. With increasing distance from the wall the flow becomes more and more isotropic, and the turbulent state approaches the isotropic state at the origin.

In figure 11 the states on the anisotropy invariant map are shown for various roughness cases using either the Gaussian or the box shape function. The other shape functions yield similar results. The values at the distances $z^+ \approx h^+$ and $z^+ \approx 2h^+$ from the wall are highlighted by a square and a circle to give an impression of the

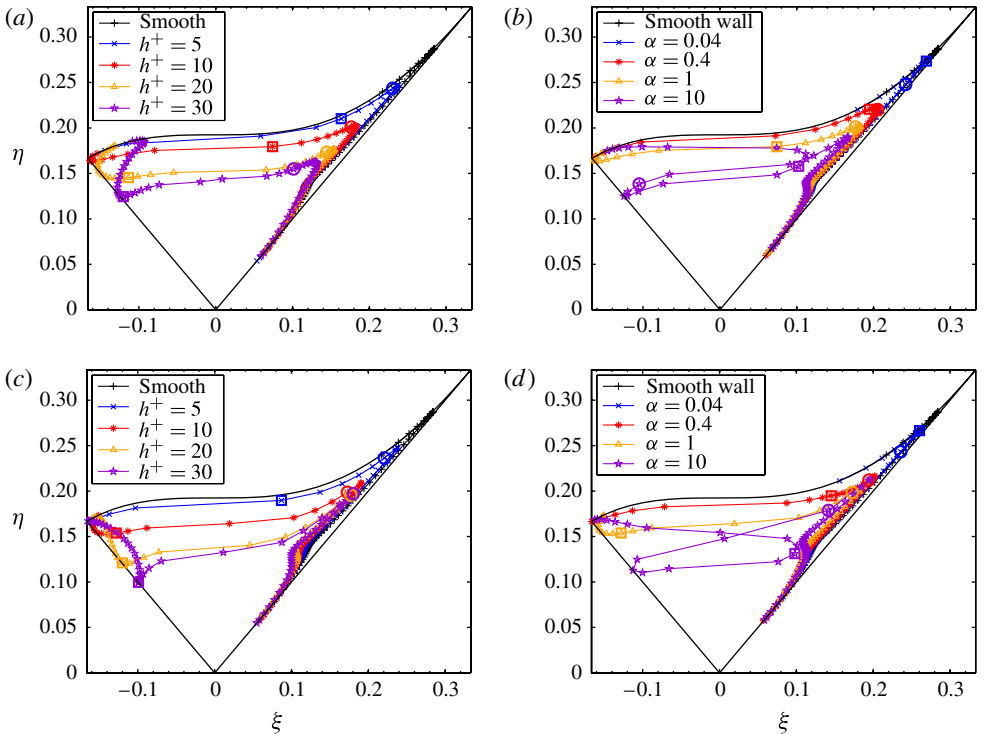

FIGURE 11. (Colour online) The anisotropy invariant map for the Reynolds stress anisotropy tensor. The black lines outline the Lumley triangle. (*a*,*b*) Cases for the Gaussian shape function. (*c*,*d*) Cases using the box shape function. (*a*,*c*) Results for different height parameters using $\alpha = 1$. (*b*,*d*) Results for different roughness factors using a constant roughness height of $h^+ = 10$. The squares and circles indicate the data points obtained at distances from the wall equal to $z^+ \approx h^+$ and $z^+ \approx 2h^+$.

position relative to the roughness layer. In the case of the box shape function, this corresponds to the middle and the top of the roughness elements. For the transitionally and fully rough cases, the turbulent state near the wall now starts near the left side of the triangle, corresponding to disc-like turbulence. This is a consequence of the fact that the streamwise velocity fluctuations are the ones most strongly damped by the roughness term; therefore near the wall the level of the streamwise velocity fluctuations approaches that of the spanwise velocity fluctuations. With increasing distance from the wall, the turbulent state crosses over from the left to the right side of the triangle, corresponding to a change from disc-like to rod-like turbulence. The peak level of anisotropy achieved (the maximum value of η) is in all cases smaller than in the reference case. Above the roughness elements, i.e. approximately beyond the points highlighted by the circles, the curves approximately collapse onto the curve for the reference case. This indicates that the anisotropy of the Reynolds stresses in the outer layer is not strongly affected by the presence of the roughness term.

In cases with extreme values of the roughness parameters (roughness height and/or roughness factor very high), the path across the anisotropy invariant map is more complicated. For high roughness heights the trajectory stays close to the left side of the triangle for a significant range of distances from the wall, consistent with a

region of mixing-layer-like turbulence near the wall. In the case of high roughness factors (and medium to high roughness heights), the trajectory crosses the Lumley triangle twice, indicating a complex change in the turbulence structure throughout the roughness layer. With regards to the outer layer, we can observe that in the case of extreme values of the roughness parameters the collapse onto the reference case is limited to locations further and further away from the wall, and in general the cases using the box shape function show a less satisfactory collapse than the ones for the Gaussian shape function.

Probably not too much importance should be placed on what happens in the region of the flow that is directly and strongly affected by the roughness term. We will therefore concentrate first on what happens outside this roughness layer, i.e. the part of each curve beyond the points highlighted by the circles. The general observation from experimental and DNS data is that the presence of the roughness changes the anisotropy in the layer near the rough surface. Most studies report a decrease of the near-wall anisotropy caused by the presence of the roughness elements (Antonia & Krogstad 2001; Smalley *et al.* 2002; Ashrafian & Andersson 2006; DeMarchis *et al.* 2010). (This applies to k-type roughnesses; there is only a very weak effect for d-type roughnesses according to Smalley *et al.* (2002).) Far away from the wall, a reasonably good collapse onto the smooth-wall case is observed in most studies (at least for turbulent channel flow), and the collapse seems to occur later for stronger roughnesses (DeMarchis *et al.* 2010). These observations are all mirrored in our data.

From DNSs the anisotropy invariant map can be obtained within the roughness elements, i.e. the cavities of the rough surfaces. Ashrafian & Andersson (2006) observed a disc-like state of the turbulence within the cavities of the rod-roughened wall they studied, not unlike that for the moderately rough cases studied here. A complex behaviour within the cavity with two crossings of the anisotropy invariant map was also observed by Smalley *et al.* (2002). Within the cavities the turbulence state will very much depend on the type and geometry of the rough surface, and it will probably not be possible to match this closely with the current model. However, it is reassuring that the behaviour induced by the roughness term is comparable with that observed in DNSs where the roughness elements are fully resolved.

The invariant function F, defined as $F = 1+9\,\mathrm{II}_b+27\,\mathrm{III}_b$, is a measure of the overall anisotropy of the Reynolds stress tensor. The function F is bounded between 0 and 1, where $F = 0$ for two-component turbulence and $F = 1$ in the case of three-dimensional isotropic turbulence. In the case of a smooth-wall channel flow, F starts from zero at the wall, where the impenetrability condition for the wall-normal component of the velocity enforces a two-dimensional turbulent state, and increases towards the middle of the channel, where the turbulent state is close to isotropy. In the logarithmic region, F is approximately constant, indicating a self-similar turbulent state (Krogstad *et al.* 2005). As can be observed from figure 12, this region is not clearly developed here, as the Reynolds number of the simulations limits the extent of the self-similar region. In the cases with roughness, the Reynolds stresses near the wall are more isotropic than the smooth-wall reference solution (see figure 12). For the cases corresponding to high roughnesses, this takes the form of a peak at $z \approx h$, i.e. in the middle of the layer directly affected by the roughness term. In the outer layer, the curves collapse approximately onto the reference case. In cases with high values of the roughness height, the collapse is less satisfactory or non-existent, whereas it is only slightly impaired for high values of the roughness factor. In fully and extremely rough cases, high values of the roughness height parameter lead to a higher degree of anisotropy in the outer layer. This is probably a low-Reynolds-number effect, as the low Reynolds

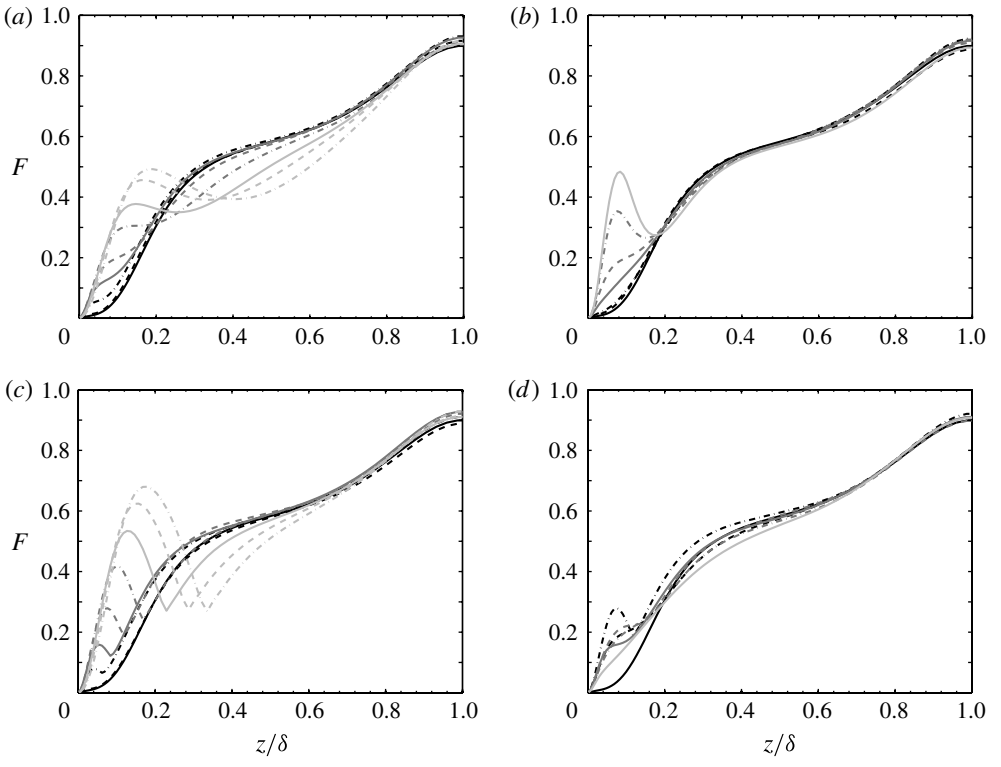

FIGURE 12. Invariant function F. (a) Gaussian shape function, $\alpha = 1$, different roughness heights (line styles as in figure 6a). (b) Gaussian shape function, $h^+ = 10$, different roughness factors (line styles as in figure 6b). (c) Box shape function, $\alpha = 1$, different roughness heights (line styles as in panel (a)). (d) Various shape functions using $\alpha = 1$, $h^+ = 10$ (line styles as in figure 8).

number used impairs the recovery of the outer-layer similarity in highly rough cases. All the shape functions studied here have the same isotropy-increasing effect near the wall (see figure 12d). Further from the wall the box and the exponentially decaying shape functions show the largest deviation from the reference case.

In simulations of rod-roughened channel flow, Krogstad *et al.* (2005) and Ashrafian & Andersson (2006) also observed an increase of the invariant function near the wall and a collapse onto the smooth-wall results in the outer layer. A peak in F near the wall was observed within the cavities of the roughness in the DNS of Ashrafian & Andersson (2006).

4.6. *Structure of the velocity field*

Rough surfaces are known to have a strong influence on the structure of the velocity field in the near-wall region. In this section the effects of the roughness force term on the structure of the velocity field are discussed based on the spatial correlation functions and length scales of the velocity field and compared to numerical and experimental observations.

As correlation statistics close to a rough wall are difficult to acquire in experiments, most observations regarding the spatial correlation of the velocity field have been obtained from DNSs. In general a decrease of the streamwise correlation of the

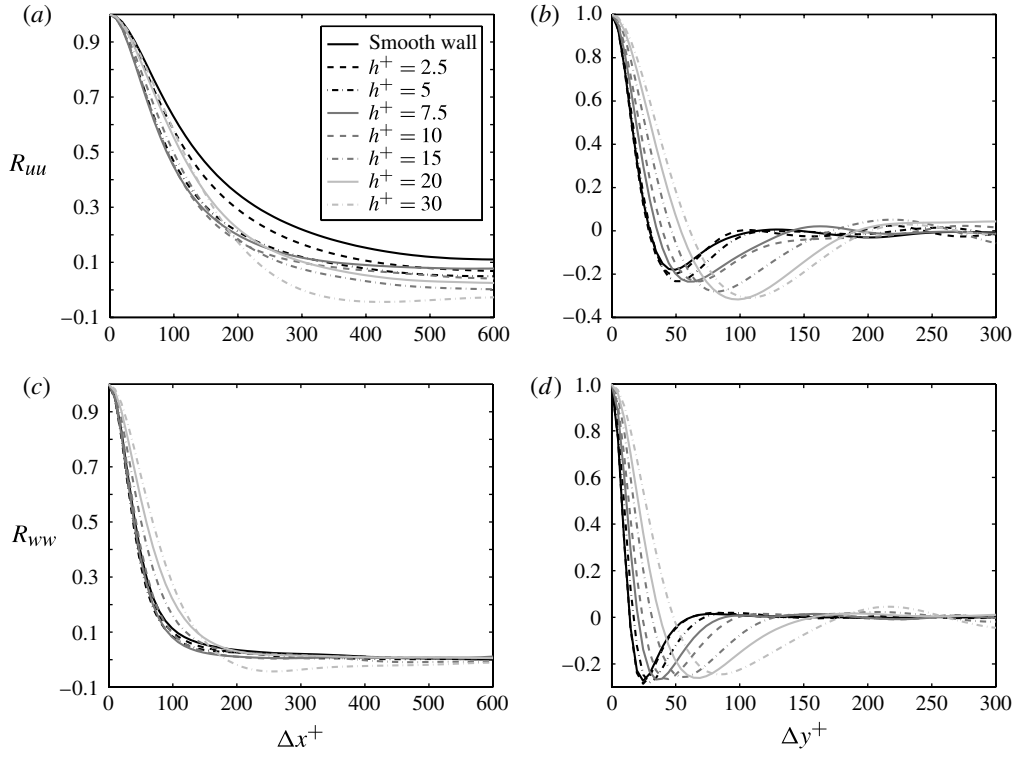

FIGURE 13. Two-point correlation measured at $z^+ \approx 2h^+$ ($z^+ = 5$ in the reference case) for the (a,b) streamwise and (c,d) wall-normal velocity components in streamwise and spanwise directions. Cases for a Gaussian shape function and a roughness factor $\alpha = 1$.

velocity field is observed in the roughness sublayer and an increase of the spanwise correlation (Bhaganagar *et al.* 2004; Leonardi *et al.* 2004; Ashrafian & Andersson 2006; DeMarchis *et al.* 2010).

In the simulations using the roughness term, some of these observations can be recovered. We will first discuss how the flow changes above the roughnesses, at a distance of approximately $z^+ = 2h^+$ from the wall (see figure 13). For comparison the correlation functions are given in the smooth-wall reference case at a distance $z^+ = 5$ from the wall. For the cases $h^+ = 2.5$ up to $h^+ = 10$ a decrease in the streamwise correlation of the streamwise velocity R_{uu} can be observed. For the higher roughness heights a reversal of this trend can be seen and the correlation increases for short distances from the wall. In these cases the correlation is still significantly lower than in the reference case. This is an indication for a weakening of the characteristic streaks in the streamwise velocity near the boundary (see figure 14). In the transverse correlation of the streamwise velocity an increase can be observed. The streamwise velocity shows in these respects for small to moderate roughness heights similar behaviour to the fully resolved DNS discussed above. However, one significant difference can be observed: the negative minimum of the spanwise correlation of the streamwise velocity increases with increasing strength of the roughness term whereas it decreases or remains approximately constant for rough-wall flows (DeMarchis *et al.* 2010; Birch & Morrison 2011), indicating that the alternating positive–negative pattern in the streamwise velocity field is weakened (Leonardi *et al.* 2004). This difference is

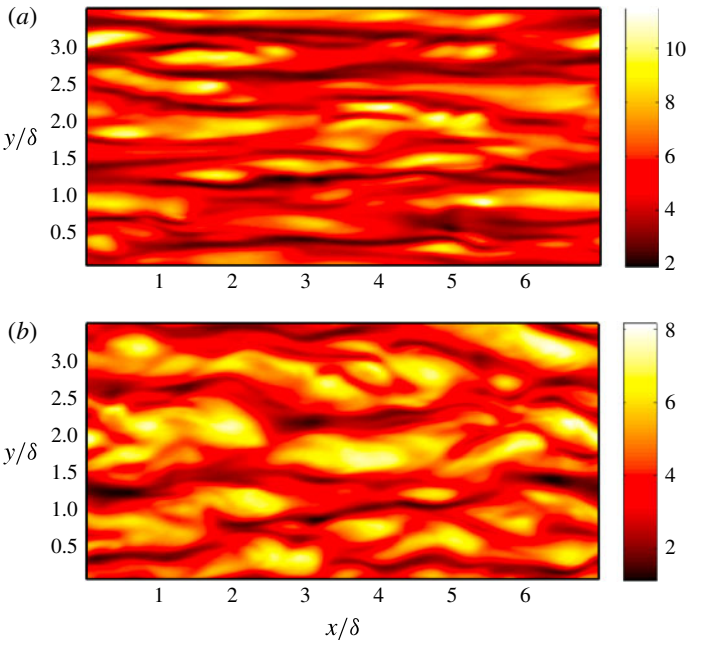

FIGURE 14. (Colour online) Contours of u for (a) smooth-wall reference case at $z^+ = 5$, and (b) case using a Gaussian shape function, $\alpha = 1$, $h^+ = 10$ at $z^+ = 20$. For the rough case, a higher distance from the wall has been chosen in order to illustrate the flow 'above' the roughnesses, i.e. at $z^+ = 2h^+$.

probably due to the damping nature of the roughness term, which does not reproduce the detailed interaction of the flow with the roughness elements, leading rather to a coarsening of the structure of the velocity field than to an increased level of small-scale structures as one would expect for a fully resolved rough surface (see e.g. figure 15 in Bhaganagar *et al.* (2004)).

For moderate strengths of the roughness term, the streamwise correlation of the wall-normal velocity is almost unchanged. For high roughnesses an increase in the streamwise correlation can be observed. In contrast, DeMarchis *et al.* (2010) observed a decrease in the streamwise correlation of the wall-normal velocity in numerical simulations of flow over an irregular wavy roughness. In the spanwise direction the correlation increases, which agrees with the expected behaviour. The differences in the streamwise correlation of the wall-normal velocity indicate that the wall-normal velocity is sensitive to processes on the scale of the individual roughness elements that are not resolved by the roughness term.

Further away from the wall the correlations length scales are of similar magnitude as the smooth-wall reference case. This is in line with general observations that the structure of turbulence is changed strongly only in the region close to the roughness elements, not in the outer layer (Ashrafian & Andersson 2006; Singh, Sandham & Williams 2007; Birch & Morrison 2011).

Within the roughness layer, i.e. below $z^+ = 2h$, the change in the spatial structure is more complex; a first indication of this was the anisotropy invariant map of the Reynolds stresses discussed in § 4.5.3. In order to get an overview of the data, a correlation length has been computed based on a 1/e measure, that

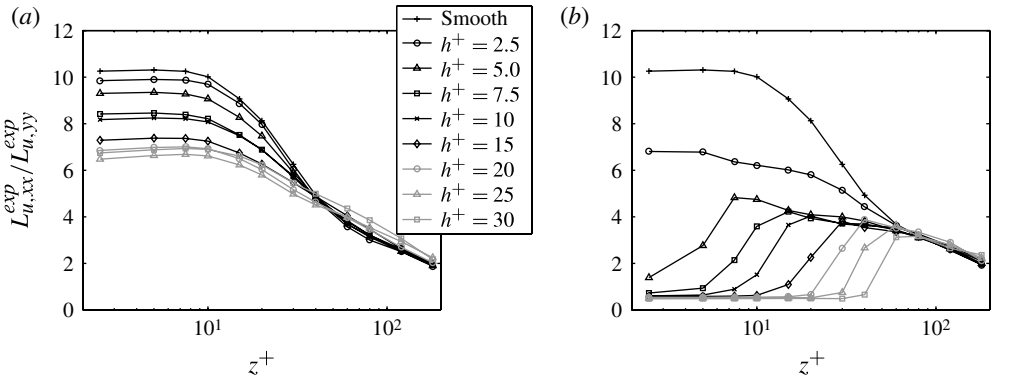

FIGURE 15. Ratio of streamwise to spanwise correlation length of streamwise velocity component: (*a*) $\alpha = 0.1$; (*b*) $\alpha = 10$; Gaussian shape function.

is $L_{u,xx} = \min\{\Delta x \mid R_{uu}(\Delta x) \leqslant 1/\mathrm{e}\}$, where $R_{uu}(\Delta x)$ is the streamwise correlation function of the streamwise velocity component; $L_{u,yy}$ is defined in an analogous way. This definition was chosen because it is less affected by numerical uncertainties than other more common definitions of correlation length scales, such as the integral length scales, and because it is defined in all cases. For the streamwise velocity component, the streamwise correlation length is nearly always reduced near the wall by the roughness term whereas the spanwise correlation length is nearly always increased. Some exceptions occur for (low α, high h^+) combinations. For the spanwise and wall-normal velocity components, both the streamwise and spanwise correlation lengths show an increase, but this is not as pronounced as for the streamwise velocity component. Near the centre of the channel the correlation lengths are of the same order of magnitude as in the smooth-wall reference case. The same trends are observed for all shape functions studied here.

In figure 15 the ratio between the streamwise and spanwise correlation lengths of the streamwise velocity is shown. In the reference case a very high aspect ratio of over 10 can be observed near the wall, indicating the presence of the long streamwise streaks in the velocity field. With increasing roughness height and increasing roughness factor, the aspect ratio decreases near the wall towards a more isotropic pattern. This is in line with the observations of Reynolds & Castro (2008) for staggered cube roughnesses where a decrease in the ratio of the streamwise to the spanwise correlation length of the streamwise velocity was observed within the roughness sublayer.

In some extremely rough cases the emergence of spanwise structures ($L_{u,xx}/L_{u,yy} < 1$) can be observed (see figures 15*b* and 16). This would agree with the observation already made from the anisotropy invariant map of the Reynolds stresses that the flow structure changes to a mixing-layer-like form near the wall. This has many properties of the flow over plant canopies, which is reminiscent of a mixing layer (Finnigan 2000). In the outer layer the structures in the streamwise velocity field show an aspect ratio similar to the smooth-wall reference case.

5. Example for a direct comparison

In the previous sections the influence of the parameters in the roughness force term on the flow has been investigated, and the comparison to experimental and DNS data

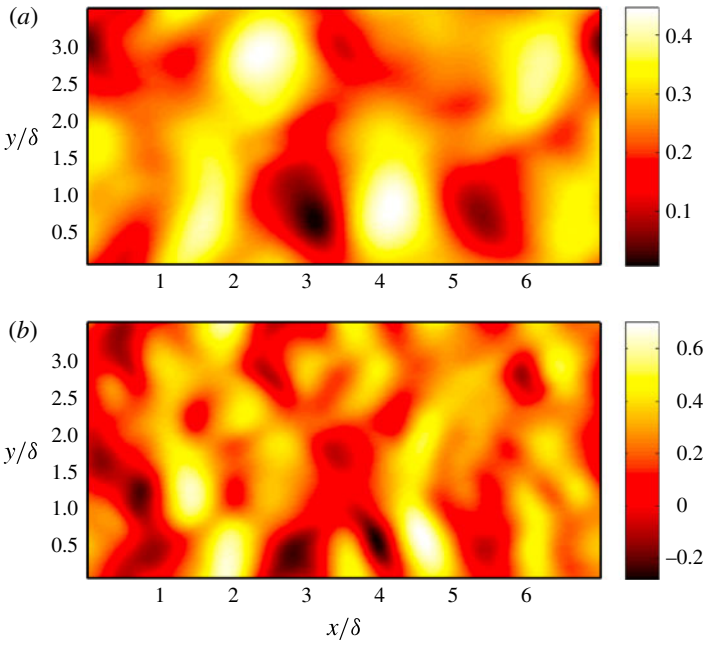

FIGURE 16. (Colour online) Contours of u at a distance of $z^+ = 10$ from the wall in two extremely rough cases ($\alpha = 10$, $h^+ = 30$): (*a*) Gaussian shape function, and (*b*) box shape function.

has necessarily been qualitative. An example of a direct quantitative comparison will be provided in this section.

To this end the case of Ashrafian, Andersson & Manhart (2004) has been chosen, which considered channel flow over a rod-roughened wall by DNSs. There are several reasons for this choice. DNS data provide a high accuracy close to the wall where experimental measurements are difficult. The DNS was conducted at a Reynolds number $Re_\tau = 400$, giving a reasonable log law but still low enough to require (nowadays) only moderate computational expense. In contrast, experiments are typically performed at higher Reynolds numbers and provide less data. The roughness geometry is fairly simple and applied to both walls, which is not the case for many other DNSs of rough-wall turbulent channel flow. Also, a similar domain size was used, $6.528\delta \times \pi\delta \times 2\delta$, which is close to the domain size of $7\delta \times 3.5\delta \times 2\delta$ used in this paper. The DNS data of Ashrafian *et al.* (2004) will be referred to as AAM in the following.

The roughness used in AAM consists of transverse square bars of a height $k^+ = 13.6$. The pitch-to-height ratio of the bars was set to 8 in order to achieve a maximum influence on the mean velocity profile; the width of the grooves between the bars is thus high enough to make this a clear k-type rough surface (Raupach, Antonia & Rajagopalan 1991; Jiménez 2004).

For the simulation of the effects of this roughness type using the roughness term, the box profile has been chosen for the roughness function, since the roughness (square bars) is neither random nor tapering. The roughness height parameter was set to $h^+ = 13.6/2$ so that the top of the roughness profile is located at $z^+ = 13.6$, matching the height of the square bars. The roughness term is applied in the

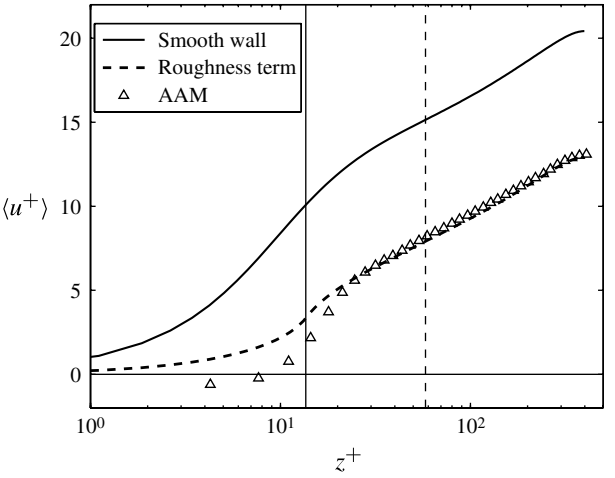

FIGURE 17. Direct comparison with AAM: mean streamwise velocity profile. The thin continuous black vertical line indicates the height of the roughness elements. The thin dashed black vertical line indicates the extent of the roughness sublayer as estimated by AAM.

streamwise direction only, so $\alpha_y = \alpha_z = 0$, mimicking the transverse orientation of the bars. The remaining free parameter, the roughness factor α, has been chosen so that a similar value of the roughness function ΔU^+ is attained, $\alpha = 6$. This comparatively high value of α reflects the optimized pitch-to-height ratio of the transverse rods chosen for AAM. Two simulations, one for the smooth-wall reference case and one for the roughness term case, have been performed using the same domain size as above, $7\delta \times 3.5\delta \times 2\delta$. A grid of size 288^3, stretched in the wall-normal direction, has been employed, giving a resolution of $\Delta x^+ = 9.72$, $\Delta y^+ = 4.86$ and $\Delta z^+_{min} = 0.73$. From a fit of the log law (for this fit, Dean's constants (Dean 1978) have been used; an estimate based on the difference in centreline velocities as used for the $Re_\tau = 180$ data (see §§ 4.1 and 4.3) would give an error of $\approx 5.6\,\%$), we obtain $\Delta U^+ = 7.1$ for the roughness term case, which is quite close to the value reported by AAM ($\Delta U^+ = 7.0$). Note that, although this choice of the roughness term is straightforward and gives satisfactory results, it is probably not the optimum one.

In figure 17 the mean streamwise velocity profile is shown. A very good agreement is observed in the outer layer and the upper part of the log layer. For $z^+ \leqslant 26$, i.e. in the lower part of the log layer and the viscous sublayer, the curves diverge. This is not surprising, as this is quite close to or below the height of the roughness elements. Note that negative velocities are attained in AAM data as recirculation regions form within the cavities. Since the roughness term depends on the wall-normal direction only, these recirculation patterns do not occur for the roughness term and thus the mean streamwise velocity remains always positive.

The Reynolds stresses are illustrated in figure 18. For AAM the profiles of the Reynolds stresses are shown at different streamwise positions above the transverse square bars. The positions $x/\lambda = 0.312,\ 0.71,\ 0.875$ are located above the cavity, and $x/\lambda = 1$ at the centre of the bars. In the figures the thickness of the roughness sublayer as estimated by AAM is shown. Outside the roughness sublayer the curves all collapse, and a good agreement is observed with the results for the roughness force term for all components of the Reynolds stress. Within the roughness sublayer some differences

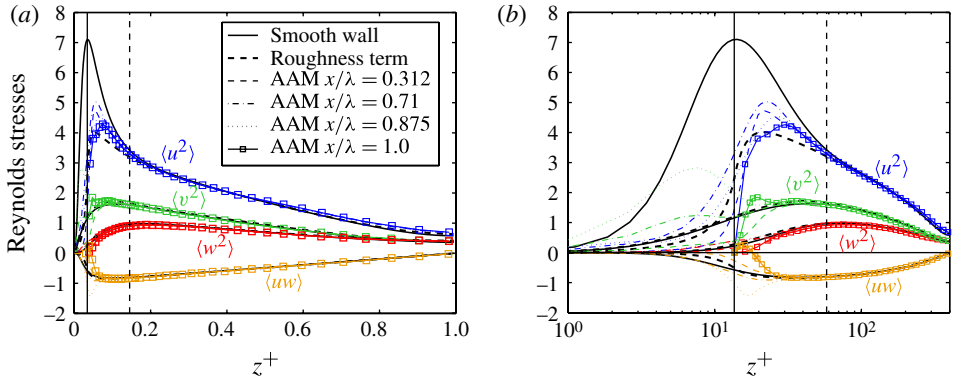

FIGURE 18. (Colour online) Direct comparison with AAM: Reynolds stresses normalized by $u_{\tau_0}^2$: (*a*) in outer coordinates, and (*b*) in inner coordinates. The thin continuous black vertical line indicates the height of the roughness elements. The thin dashed black vertical line indicates the extent of the roughness sublayer as estimated by AAM.

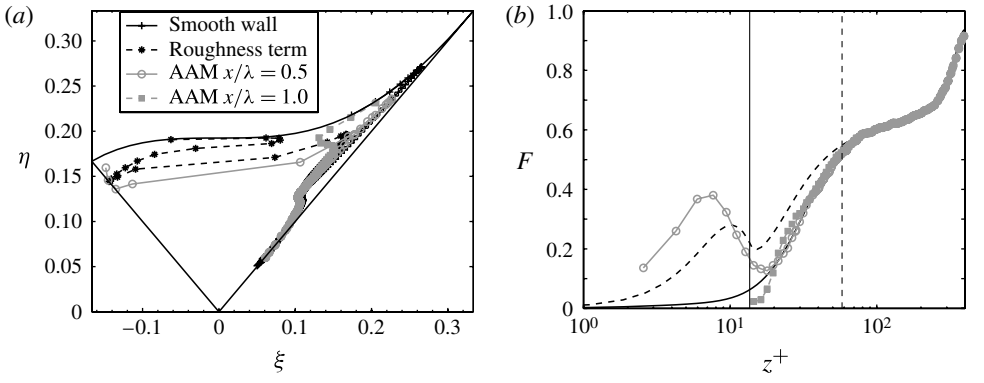

FIGURE 19. Direct comparison with AAM: anisotropy of the Reynolds stresses: (*a*) anisotropy invariant map, and (*b*) invariant F. The thin continuous black vertical line indicates the height of the roughness elements. The thin dashed black vertical line indicates the extent of the roughness sublayer as estimated by AAM.

can be observed. The peak value of the streamwise Reynolds stress is underpredicted by the roughness term. The difference is of the order of 10–20 %. As the peak value is located quite close to the top of the roughness elements, and shows a significant dependence on the streamwise position, that is not unexpected. The location of the peak streamwise Reynolds stress is at about $z^+ = 22$. This is within the variation of the position dependence of the AAM data.

The spanwise, wall-normal and shear stresses show a good agreement for $z^+ \geqslant 40$. Close to or within the rough surface, where the AAM data show a dependence on the streamwise position x/λ, the results for the roughness term fall within the range of the AAM data.

The Reynolds stress anisotropy tensor b_{ij} for the data of AAM has been reported in Ashrafian & Andersson (2006). Using these data the anisotropy invariant map and the invariant F, both shown in figure 19, have been computed. Here the data of AAM are shown at two different streamwise positions, at the mid-cavity position $x/\lambda = 0.5$

and the mid-crest position $x/\lambda = 1.0$. Within the cavities the turbulence is close to a disc-like axisymmetric turbulent state. This feature is recovered by the roughness term. With increasing distance from the wall, the turbulent state crosses over to a rod-like axisymmetric state, corresponding to the right side of the Lumley triangle. This is recovered as well. For even higher distances from the wall, all curves collapse onto the smooth-wall reference case. The invariant F facilitates a quantitative comparison. In the mid-cavity data of AAM a peak close to the wall can be observed. A similar feature occurs for the simulation with the roughness term. Above the height of the roughness elements the roughness term gives a slightly higher degree of isotropy than the AAM data. This can be attributed to the lower value of the streamwise Reynolds stress in this region. A very good match is obtained outside the roughness sublayer, where all data collapse on the smooth-wall reference case.

In conclusion, a good quantitative match is achieved outside the roughness sublayer, and a good qualitative match even within this layer. Naturally, the dependence on the streamwise position cannot be recovered, as the roughness term depends (explicitly) only on the wall-normal coordinate.

6. Conclusions

The addition of an extra body force term to the Navier–Stokes equations has been shown to model many of the effects of roughness on turbulent flow near solid boundaries, without having to resolve the details of the surface. By appropriate variations in two roughness parameters and a shape function, a range of turbulence characteristics near the wall can be captured, in particular variations in the mean profile and turbulence anisotropy near the top of the roughness elements. All but extremely rough cases show a good collapse of the mean flow in outer scaling. The variation of ΔU^+ with the roughness height parameter for a given roughness factor and shape function can be mapped onto the fully rough scaling with an appropriate equivalent sand grain roughness, derived via a nonlinear relationship. Departure from the fully rough solution for extremely rough surfaces is attributed to the reduced Reynolds number of the simulations. That the departure only occurs for $\Delta U^+ > 10$ as well as the very good preservation of the outer-layer similarity of the mean streamwise velocity and the streamwise normal stress profiles suggest that this Reynolds number is nevertheless high enough to capture representative phenomena. In the transitionally rough region the simulation ΔU^+ values span a range from just above Nikuradse's sand grain experiments up to the Colebrook curve for commercial pipes. For an alternative forcing where only the spanwise disturbances are damped, a drag reduction is seen, consistent with a potential application to riblets.

Some details of the turbulent behaviour near roughness have been examined, in particular by analysis of the anisotropy invariant map and the two-point correlation functions. The turbulence structure for extremely rough cases changes from rod-like to disc-like within the roughness sublayer. Taken together with the observation that the ratio of streamwise-to-spanwise correlation lengths changes from around 10 for smooth walls to a value below unity in very rough cases, this suggests a change to more mixing-layer-like behaviour. Indeed, the box-shape roughness is a good candidate for modelling the effect of plant canopies, for which a known effect is the emergence of mixing-layer behaviour, including spanwise-coherent structures near the top of the roughness.

The fact that a simple force term is sufficient to capture a wide range of roughness phenomena helps in the physical understanding of the flow over rough surfaces. The

streamwise drag component is clearly the dominant contribution to the roughness effects. In contrast, the spanwise drag component leads to a reduction of the roughness effects. The shape function has a comparatively weak influence on ΔU^+ but strongly influences the shape of the mean velocity profile within the roughness sublayer. Details of the flow over a rough surface such as the eddy-shedding process mainly influence the spatial structure of the turbulence for moderate roughness heights. The outer-layer similarity is maintained for all but extremely rough surfaces where the low Reynolds number interferes with the recovery in the outer layer. This implies that, if an impaired outer-layer similarity is found for a rough surface, this is caused by complex processes within the rough surface such as eddy shedding, flow reattachment, etc., which are not captured by the roughness term.

For practical applications as a rough-wall model in a simulation setting (for example, in a large-eddy simulation), the model proposed here would need to be calibrated against experiments or against DNSs in which the full detail of the surface is resolved. The two model parameters are a roughness height and a roughness factor, analogous to a roughness density. The additional shape function has a small but noticeable effect and can be used to fine-tune the turbulence characteristics in the roughness layer. A possible approach would be to do this calibration exercise for simple flows (either channel flow simulations or pipe flow experiments) and then apply the derived roughness height, roughness factor and shape function to more complex flows where it is unrealistic to expect simulations to resolve the roughness for the foreseeable future. Careful checking would need to be done in case there are additional Reynolds-number effects. Another challenge is to extract the parameters and shape function from the morphology of the surface, such as could be measured using various microscopy approaches. Both this exercise and the aforementioned calibration exercise require many more DNSs of rough surfaces where the wall geometry is resolved, probably down to the order of a viscous wall unit.

An example of a detailed comparison with independent, fully resolved rough-wall data has been provided to demonstrate the practical applicability of this approach. Using the roughness force term, a good quantitative match is achieved outside the roughness sublayer. Within the roughness sublayer, a satisfactory qualitative representation of the data is obtained.

The main area where the present model is not expected to give such a good representation of reality is the small-scale structure of the turbulent flow in the roughness sublayer, i.e. on length scales of the order of the roughness elements and below. Roughness elements are known to pump energy into the turbulence at the scale of the roughness (Hong, Katz & Schultz 2011), e.g. by vortex shedding behind the elements. This turbulence would then swell the turbulent cascade down to the dissipation range. Since individual roughness elements are not resolved by the present model, this effect is lost. Nevertheless, this omission seems a modest price to pay for a simple model that reproduces a wide range of roughness phenomena without needing to resolve individual roughness elements.

Acknowledgements

The support of the Engineering and Physical Sciences Research Council under grant numbers EP/G058318/1 and EP/G069581/1 is gratefully acknowledged. The authors would like to thank Professor I. P. Castro for helpful comments on the manuscript.

Re_τ	U_c	$\overline{U}$	δ^*	θ	H
180	18.4	15.8	0.143	0.088	1.62

TABLE 2. Mean quantities for smooth-wall reference case.

Shape function	α/h^+	2.5	5	7.5	10	15	20	25	30
Gaussian	0.04	18.3	18.0	17.3	16.6	15.1	13.9	12.8	12.0
Gaussian	0.1	18.3	17.5	16.3	15.0	13.0	11.6	10.5	9.6
Gaussian	0.4	18.0	15.9	13.7	12.2	10.0	8.5	7.5	6.6
Gaussian	1	17.5	14.4	12.0	10.4	8.4	7.1	6.3	5.6
Gaussian	4	16.2	12.3	10.0	8.6	7.1	6.0	5.2	4.6
Gaussian	10	15.2	11.3	9.4	8.1	6.6	5.7	4.9	4.3
Box	0.04	18.3	17.8	17.2	16.1	14.6	13.1	12.1	11.3
Box	0.1	18.3	17.3	16.1	14.5	12.6	10.9	9.7	8.9
Box	0.4	18.0	15.5	13.7	11.8	9.8	8.4	7.4	6.8
Box	1	17.6	14.2	12.3	10.4	8.7	7.5	6.7	6.1
Box	4	16.8	12.6	10.9	9.4	8.0	6.9	6.2	5.7
Box	10	16.2	12.3	10.8	9.4	8.1	7.1	6.4	5.9
Orbital	1	17.9	15.2	12.9	11.2	9.1	7.7	6.9	6.1
Triangular	1	17.7	14.4	12.1	10.5	8.5	7.3	6.3	5.7
Parabolic	1	17.7	14.5	12.2	10.6	8.6	7.3	6.4	5.7
Exp. decaying	1	17.5	14.8	12.5	11.0	8.9	7.5	6.7	5.8

TABLE 3. Centreline velocity U_c for the cases studied in the main parameter study.

Appendix. Simulations

Characteristic mean flow quantities are given for the smooth-wall reference case in table 2. The centreline velocities for the cases studied in the main parameter study are listed in table 3.

REFERENCES

AMIR, M. & CASTRO, I. P. 2011 Turbulence in rough-wall boundary layers: universality issues. *Exp. Fluids* **51** (2), 313–326.

ANDERSON, W. & MENEVEAU, C. 2010 A large-eddy simulation model for boundary-layer flow over surfaces with horizontally resolved but vertically unresolved roughness elements. *Boundary-Layer Meteorol.* **137**, 397–415.

ANTONIA, R. A. & KROGSTAD, P.-A. 2001 Turbulence structure in boundary layers over different types of surface roughness. *Fluid Dyn. Res.* **28**, 139–157.

ARNFIELD, A. J. 2003 Two decades of urban climate research: a review of turbulence, exchanges of energy and water, and the urban heat island. *Intl J. Climatol.* **23** (1), 1–26.

ASHRAFIAN, A. & ANDERSSON, H. I. 2006 The structure of turbulence in a rod-roughened channel. *Intl J. Heat Fluid Flow* **27**, 65–79.

ASHRAFIAN, A., ANDERSSON, H. I. & MANHART, M. 2004 DNS of turbulent flow in a rod-roughened channel. *Intl J. Heat Fluid Flow* **25**, 373–383.

BAKKEN, O. M., KROGSTAD, P. A., ASHRAFIAN, A. & ANDERSSON, H. I. 2005 Reynolds number effects in the outer layer of the turbulent flow in a channel flow with rough walls. *Phys. Fluids* **17**, 065101.

BATCHELOR, G. K. 1967 *An Introduction to Fluid Dynamics*. Cambridge University Press.

BECHERT, D. W., BRUSE, M., HAGE, W., VANDERHOEVEN, J. G. T. & HOPPE, G. 1997 Experiments on drag-reducing surfaces and their optimization with an adjustable geometry. *J. Fluid Mech.* **338**, 59–87.

BHAGANAGAR, K., KIM, J. & COLEMAN, G. 2004 Effect of roughness on wall-bounded turbulence. *Flow Turbul. Combust.* **72**, 463–492.

BIRCH, D. M. & MORRISON, J. F. 2011 Similarity of the streamwise velocity component in very-rough-wall channel flow. *J. Fluid Mech.* **668**, 174–201.

BRADSHAW, P. 2000 A note on 'critical roughness height' and 'transitional roughness'. *Phys. Fluids* **12** (6), 1611–1614.

BREUGEM, W. P. & BOERSMA, B. J. 2005 Direct numerical simulations of turbulent flow over a permeable wall using a direct and a continuum approach. *Phys. Fluids* **17**, 025103.

CASTRO, I. P. 2007 Rough-wall boundary layers: mean flow universality. *J. Fluid Mech.* **585**, 469–485.

CASTRO, I. P. 2009 Turbulent flow over rough walls. In *Advances in Turbulence XII – Proceedings of the 12th EUROMECH European Turbulence Conference* (ed. B Eckhardt). *Springer Proceedings in Physics*, vol. 132, pp. 381–388.

CHAN-BRAUN, C., GARCIA-VILLALBA, M. & UHLMANN, M. 2011 Force and torque acting on particles in a transitionally rough open-channel flow. *J. Fluid Mech.* **684**, 441–474.

CHENG, H. & CASTRO, I. P. 2002 Near wall flow over urban-like roughness. *Boundary-Layer Meteorol.* **104** (2), 229–259.

CHOI, H., MOIN, P. & KIM, J. 1993 Direct numerical simulations of turbulent flow over riblets. *J. Fluid Mech.* **255**, 503–539.

COCEAL, O. & BELCHER, S. E. 2005 Mean winds through an inhomogeneous urban canopy. *Boundary-Layer Meteorol.* **115**, 47–68.

CUI, J., PATEL, V. C. & LIN, C.-L. 2003 Prediction of turbulent flow over rough surfaces using a force field in large eddy simulations. *J. Fluids Engng* **125**, 2–9.

DEAN, R. B. 1978 Reynolds number dependence of skin friction and other bulk flow variables in two-dimensional rectangular duct flow. *Trans. ASME* I: *J. Fluids Engng.* **100**, 215.

DEANGELIS, V., LOMBARDI, P. & BANERJEE, S. 1997 Direct numerical simulation of turbulent flow over a wavy wall. *Phys. Fluids* **9** (8), 2429–2442.

DEMARCHIS, M., NAPOLI, E. & ARMENIO, V. 2010 Turbulence structure over irregular rough surfaces. *J. Turbul.* **11** (3), 1–32.

FINNIGAN, J. 2000 Turbulence in plant canopies. *Annu. Rev. Fluid Mech.* **32**, 519–571.

FLORES, O. & JIMÉNEZ, J. 2006 Effects of wall-boundary disturbances on turbulent channel flow. *J. Fluid Mech.* **566**, 357–376.

HAMA, F. R. 1954 Boundary-layer characteristics for smooth and rough surfaces. *Trans. Soc. Nav. Arch. Marit. Engrs* **62**, 333–351.

HONG, J., KATZ, J. & SCHULTZ, M. P. 2011 Near-wall turbulence statistics and flow structures over three-dimensional roughness in a turbulent channel flow. *J. Fluid Mech.* **667**, 1–37.

HU, Z. W., MORFEY, C. L. & SANDHAM, N. D. 2006 Wall pressure and shear stress spectra from direct simulations of channel flow. *AIAA J.* **44** (7), 1541–1549.

ICCARINO, G. & VERZICCO, R. 2003 Immersed boundary technique for turbulent flow simulations. *Appl. Mech. Rev.* **56**, 331–347.

JIMÉNEZ, J. 2004 Turbulent flow over rough walls. *Annu. Rev. Fluid Mech.* **36**, 173–196.

KARNIADAKIS, G. E. & CHOI, K.-S. 2003 Mechanisms on transverse motions in turbulent wall flows. *Annu. Rev. Fluid Mech.* **35**, 45–62.

KROGSTAD, P.-A., ANDERSSON, H. I., BAKKEN, O. M. & ASHRAFIAN, A. 2005 An experimental and numerical study of channel flow with rough walls. *J. Fluid Mech.* **530**, 327–352.

LANGELANDSVIK, L. I., KUNKEL, G. J. & SMITS, A. J. 2008 Flow in a commercial steel pipe. *J. Fluid Mech.* **595**, 323–339.

LEE, J. H., SUNG, H. J. & KROGSTAD, P.-A. 2011 Direct numerical simulation of the turbulent boundary layer over a cube-roughened wall. *J. Fluid Mech.* **669**, 397–431.

LEONARDI, S. & CASTRO, I. P. 2010 Channel flow over large cube roughness: a direct numerical simulation study. *J. Fluid Mech.* **651**, 519–539.

LEONARDI, S., ORLANDI, P., DJENIDI, L. & ANTONIA, R. A. 2004 Structure of turbulent channel flow with square bars on one wall. *Intl J. Heat Fluid Flow* **25**, 384–392.

LUMLEY, J. L. 1978 Computational modelling of turbulent flows. *Adv. Appl. Mech.* **18**, 123–176.

MARUSIC, I., MCKEON, B. J., MONKEWITZ, P. A., NAGIB, H. M. & SMITS, A. J. 2010 Wall bounded turbulent flows at high Reynolds numbers: recent advances and key issues. *Phys. Fluids* **22**, 065103.

MITTAL, R. & ICCARINO, G. 2005 Immersed boundary methods. *Annu. Rev. Fluid Mech.* **35**, 239–261.

MOSER, R. D., KIM, J. & MANSOUR, N. N. 1999 Direct numerical simulation of turbulent channel flow up to $Re_\tau = 590$. *Phys. Fluids* **11** (4), 943–945.

NIKURADSE, J. 1950 Laws of flow in rough pipes. *Tech. Rep.* NACA Technical Memorandum 1292.

ORLANDI, P., LEONARDI, S., TUZI, R. & ANTONIA, R. A. 2003 Direct numerical simulation of turbulent channel flow with wall velocity disturbances. *Phys. Fluids* **15**, 3587–3601.

POPE, S. B. 2000 *Turbulent Flows*. Cambridge University Press.

RAUPACH, M. R., ANTONIA, R. A. & RAJAGOPALAN, S. 1991 Rough-wall turbulent boundary layers. *Appl. Mech. Rev.* **44**, 1–25.

REYNOLDS, R. T. & CASTRO, I. P. 2008 Measurements in an urban-type boundary layer. *Exp. Fluids* **45**, 141–156.

ROTHSTEIN, J. P. 2010 Slip on superhydrophobic surfaces. *Annu. Rev. Fluid Mech.* **42**, 89–109.

SCHLICHTING, H. 1968 *Boundary-Layer Theory*, 6th edn. McGraw-Hill.

SCHULTZ, M. P. & FLACK, K. A. 2009 Turbulent boundary layers on a systematically varied rough wall. *Phys. Fluids* **21**, 015104.

SCOTTI, A. 2006 Direct numerical simulation of turbulent channel flows with boundary roughened with virtual sandpaper. *Phys. Fluids* **18**, 031701.

SIMONSEN, A. J. & KROGSTAD, P. A. 2005 Turbulent stress invariant analysis: clarification of existing terminology. *Phys. Fluids* **17**, 088103.

SINGH, K. M., SANDHAM, N. D. & WILLIAMS, J. J. R. 2007 Numerical simulation of flow over a rough bed. *J. Hydraul. Engng ASCE* **133**, 386–398.

SMALLEY, R. J., LEONARDI, S., ANTONIA, R. A., DJENIDI, L. & ORLANDI, P. 2002 Reynolds stress anisotropy of turbulent rough wall layers. *Exp. Fluids* **33**, 31–37.

TAYLOR, R. P., COLEMAN, H. W. & HODGE, B. K. 1985 Predicition of turbulent rough-wall skin friction using a discrete element approach. *J. Fluids Engng* **107**, 251–257.

TUCK, E. O. & KOUZOUBOV, A. 1995 A laminar roughness boundary condition. *J. Fluid Mech.* **300**, 59–70.

XIE, Z.-T., COCEAL, O. & CASTRO, I. P. 2008 Large-eddy simulation of flows over random urban-like obstacles. *Boundary-Layer Meteorol.* **129**, 1–23.